Quantitative Susceptibility Mapping and Cognitive Impairment in Parkinson 's Disease

Masters Thesis
5th May 2017

James Small
MSc in Medical Physics
Department of Physics & Astronomy
University of Canterbury

Supervisors

Dr. Steven Marsh
Director of Medical Physics,
Department of Physics and Astronomy,
The University of Canterbury
steven.marsh@canterbury.ac.nz

Dr. Tracy Melzer
MRI Research Manager
New Zealand Brain Research Institute
tracymelzer@otago.ac.nz

New Zealand Brain Research Institute

Table of Contents

List of Figures

List of Tables

Acknowledgements

Firstly I'd like to thank my supervisors, Dr. Steven Marsh and Dr. Tracy Melzer, for giving me the opportunity to undertake this study and providing amazing support throughout. Tracy has been an incredible supervisor right from day one. I've learnt so much about image processing from under his guidance and couldn't have done the analyses without him. Steve has been great from an administrative perspective keeping me up to date with deadlines and requirements in order to meet the needs of the thesis and keeping me in the loop with regards to seminars and conferences.

I'd personally like to thank the following members of the New Zealand Brain Research Institute (NZBRI) who directly or indirectly aided this research; Kyla-Louise Wood, Leslie Livingston and all of the recruitment team that have assessed patients and collated all the patient data, this study would literally not be possible without them and their efforts, Daniel Myall for his help with, and development of, the statistical analyses, Reza for his assistance with Linux batch processing, Dr. Michael McAskill for his assistance with R programming and Mildred Tan whom I shared several pre-processing tasks with in the early stages. I'd like to thank our partners, at the University of Cornell, who provided the basis for the MATLAB code used to create the quantitative susceptibility maps.

I'd like to thank my Aunt Sue and Uncle Steve for accommodating me these past two years and for all their hospitality along with proof reading and feedback for this thesis.

Finally I'd like to thank my family, especially my parents Gina & Peter and my partner Kim for supporting my academic pursuits and putting up with my prolonged absence whilst I have been away from home studying in Christchurch, this work is dedicated to all of you.

Abstract

Excess iron deposition in the substantia nigra (SN) has been linked to Parkinson's disease (PD). Increased iron deposition may also be associated with PD duration and worsening motor impairment. Iron deposition in the SN and the almost inevitable progression to dementia in PD has not yet been investigated. Furthermore the link between PD with normal cognition (PD-N), those with mild cognitive impairment (PD-MCI) and dementia (PDD) and excess iron deposition in key grey matter nuclei of the basal ganglia (BG) other than the SN may be even more pertinent. In this thesis, I use a non-invasive, magnetic resonance imaging (MRI) methodology called quantitative susceptibility mapping (QSM) to indirectly estimate iron deposition in these grey matter nuclei and determine whether QSM values are associated with cognitive impairments in PD.

A total of 121 subjects were recruited for this study. Extensive neuropsychological testing was used to characterize participants. Of these 31 were PD-N, 56 were PD-MCI, 10 were PDD and 24 were age and sex matched healthy controls (HCs). Subjects were imaged using a multi-echo spoiled gradient echo. QSM was reconstructed from the raw images using non-linear morphology enabled dipole inversion and Laplacian boundary value background field removal. QSM values were extracted from the BG and red nucleus (RN) using two separate segmentations. Bayesian multi-level regression models were used to (1) test for differences between HCs and PD as a whole in each region of interest (ROI), and (2) to investigate any association between QSM values and cognitive impairment. Finally a whole brain analysis was performed to assess group differences on a voxel-by-voxel association between QSM values and cognitive score.

Relative to controls, the PD group showed significantly higher QSM values in the SNc. There were no significant group differences in QSM values across the other basal ganglia structures investigated. For the category analysis the left SNc for PD-N was the only significant difference observed. There was a weak positive correlation between the right RN and cognitive score with no other nuclei having any significant correlation. Whole brain analyses revealed no significant differences between the groups or association with cognition.

In this thesis, I confirmed that increased QSM, and hence iron accumulation, in SNc in PD is a robust finding, consistent with previous imaging and pathological studies on PD, however this finding was limited to the ROI analysis. It appears from the evidence we have gathered that iron deposition does not affect cognitive functioning. In conclusion, this thesis established QSM in a population of PD patients. While the group association agreed with past studies this thesis hints a number of possible improvements and new directions to further investigate cognition and QSM.

Glossary of Terms

α: flip angle
δ: local magnetic field map
χ: magnetic susceptibility
B_0: main magnetic field
BFR: background field removal
BG: basal ganglia
CogZ: cognitive z-score
DICOM: Digital Imaging and Communications in Medicine
EM: electromagnetic
FWHM: full width half maximum
FSL: FMRIB Software Library
GP: globus pallidus
HC: healthy control
LBV: Laplacian boundary value
MDSTF: Movement Disorders Society Task Force
MEDI: morphology enabled dipole inversion
MNI: Montreal Neurological Institute
MR: magnetic resonance
MRI: magnetic resonance imaging
M_{xy}: transverse magnetisation
M_z: longitudinal magnetisation
NIFTI: Neuroimaging Informatics Technology Initiative
NZBRI: New Zealand Brain Research Institute
PD: Parkinson's disease
PDF: projection onto dipole fields
PD-MCI: mild cognitive impairment in Parkinson's disease
PDD: Parkinson's disease dementia
ppm: parts per million
QS: quantitative susceptibility
QSM: quantitative susceptibility mapping
RF: radiofrequency
ROI: region of interest
SPGRE: spoiled gradient echo
SPM: Statistical Parametric Mapping
SN: substantia nigra
SNc: substantia nigra pars compacta
SNr: substantia nigra pars reticulata
SNR: signal to noise ratio
TE: echo time
TR: repetition time.
UPDRS: Unified Parkinson's Disease Rating Scale

Chapter 1: Introduction

1.01 Introduction to Parkinson 's Disease & its Impact on Society

Parkinson's disease (PD) is a neurodegenerative disease that, like many diseases, is named after the man who first identified it, James Parkinson, in 1817 who originally called PD "Shaking Palsy" [(1)]. He observed and noted the classic motor symptoms of PD; rest tremor of 4-6Hz, asymmetrical and insidious onset, Bradykinesia or slowness of movement, stiffness, flexed posture and a 'festinating gait' [(1)].

PD has since been recognised as the second most common neurodegenerative disease in the world after Alzheimer's [(2)]. 3% of the New Zealand population over 65 years of age, approximately 10,000 individuals, are diagnosed with the disease [(3)]. PD however is not exclusive to the elderly with 10% of PD patients in New Zealand being under the age of 40 [(3)]. Currently 16% of the population in New Zealand is over 65 and that is estimated to grow to 25% by the year 2041 [(4)]. With a growing ageing population caused by sub-replacement fertility, increasing life expectancy and the passage of baby boomers into retirement ages, PD is becoming an increasing burden in terms of the quality of life of its sufferers and their loved ones and in terms of the financial burden of the disease on the state [(4)]. As a result there is increasing demand and pressure to develop treatments and interventions for PD and its subtypes [(5)]. In a recent report from the Ministry of Health, the government voiced their concerns stating,

"*We may be living longer, and living longer in good health, but we are also living longer in poor health. Our health system and wider society have proved more adept at preventing early death than at avoiding or ameliorating morbidity. A greater focus on addressing the impact of non-fatal disabling conditions, whether through prevention or improved management, will enable people to live more of their 'extra' years of life in full health… Neuropsychiatric disorders are now the leading cause of health loss, accounting for 19% of total disability-affected life years (DALYs).*" [(5)]

In an ironic twist it was found that improving healthcare actually increased the cost of healthcare expenditure rather than decreased it due to the population living longer in morbidity [(5)].

1.02 Parkinson's Disease Anatomy and Physiology

In order to understand Parkinson's disease one must first understand the basal ganglia (BG). The BG is a collection of grey matter nuclei that together help regulate the initiation and execution of voluntary movement and thought [(6)]. The primary components of the BG are the caudate nucleus,

the putamen, the globus pallidus (GP), the thalamus and the substantia nigra (SN) (fig. 1.01) [6]. The SN and GP are further divided into two segments, the SN pars compacta (SNc) and pars reticulata (SNr) and the internal and external globus pallidus (fig. 1.01) [6].

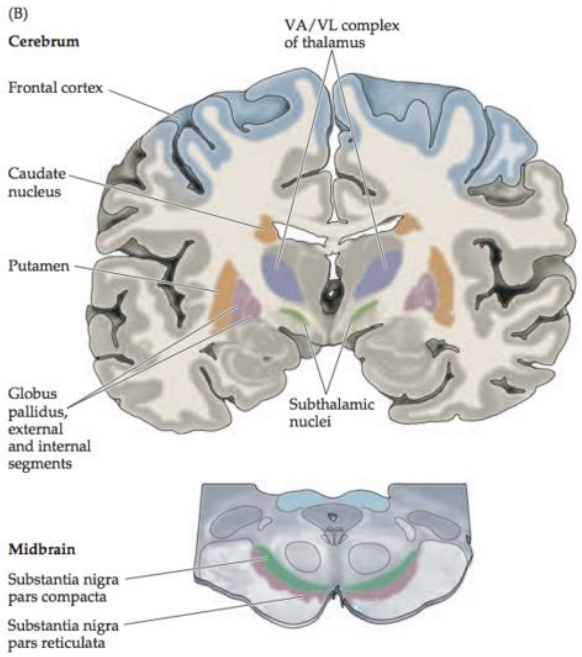

Figure 1.01: Anatomy of the basal ganglia (BG) [6]. The BG is primarily comprised of the caudate nucleus, putamen, globus pallidus (GP), thalamus and substantia nigra (SN) which lie just below the subthalamic nuclei. The GP is further divided into two segments, the internal and external GP and the SN, into the pars compacta (SNc) and pars reticulata (SNr) [6]. The SNc supplies the caudate nucleus and putamen with the neurotransmitter dopamine allowing the BG as a whole to regulate voluntary motor and cognitive neural networks [6].

The SNc provides the caudate nucleus and putamen (collectively called the dorsal striatum) with the neurotransmitter dopamine [6]. The SNc isn't the only provider of dopamine in the brain, but it is the only group of neurones that provides the dorsal striatum with dopamine [6]. Dopamine has affinities for specific G-protein-coupled receptor sites found in the dorsal striatum [6]. Binding to these receptor sites either inhibits or excites adenylyl cyclase, which in turn contributes to a large number of complex behaviours [6]. The dorsal striatum primarily mediates motor function, specifically the inhibition and initiation of voluntary motor pathways [6] and also is involved in some prefrontal and limbic neural loops, which control or contribute to a wide variety of executive functions, and stimulus-response learning [6].

PD is associated with the death of neurones in the SNc [6]. The subsequent lack of dopamine causes the motor symptoms attributed to PD, however dopamine produced by SNc is also involved in a variety of complex cognitive, thought, mood and behavioural functions, which are also impacted [6]. Examples of non-motor symptoms related to PD include, REM sleep disturbance, sensory deficits particularly smell, depression, anxiety, speech deficits and cognitive deficits such as deficits in learning, attention, memory, working memory, judgment and evaluation, reasoning, problem solving and decision making, planning, visuospatial processing, cognitive flexibility and abstract thinking [6]. SNc cell loss has only been attributed to some of these functions and it is thought that the degradation of other nuclei in the BG may account for the rest of these non-motor symptoms.

The main cause of SNc cell loss is still largely unknown or idiopathic and it is not known exactly what causes these dopaminergic neurones to undergo apoptosis or programmed cell death [6]. Mutations of three distinct genes; PINK-1, DJ-1 and Parkin have been found to cause PD, but only in rare cases and they account for a very small minority, less than 1% [6, 7]. Cell death has been associated with metabolic dysfunction and abnormalities in the mitochondrial complex-1 gene, which is the primary difference between the SNc and the other dopaminergic regions of the brain that don't undergo spontaneous cell death [8]. It is proposed that SNc is also particularly vulnerable to the aggregation and accumulation of α-synuclein proteins, due to possessing long, thin and poorly myelinated axons, which has become the pathological hallmark of the disease [9]. Another signature of PD is iron deposition. The first link between iron deposition in the brain and PD was noted in 1987 when Dexter et al identified an abnormally high iron content of the SNc in post mortem brains of people who had died as a result of PD [10]. Iron is a cofactor in the production of L-DOPA, the immediate precursor to dopamine however excess iron can produce harmful free radicals [11]. Iron accumulation in PD has been found to cause harmful oxidative stress, metabolic dysfunction and promotion of α-synuclein aggregation that could be the primary cause of neuronal cell death [12, 13]. It is unclear however as to whether improper regulation of iron transport and storage is the cause of accumulation or whether it is a consequence of neurodegeneration initiated by other means.

1.03 Cognitive Impairment in Parkinson's Disease

Many patients with PD will also develop cognitive impairments, in addition to their motor symptoms. Relatively minor cognitive impairment is referred to as mild cognitive impairment in PD (PD-MCI) [14]. Some PD-MCI patients may experience visual hallucinations along with further sudden decline in multiple areas of cognition, which if significantly impacted, will result in dementia (known as PD dementia or PDD) [15]. PD-MCI is graded between normal cognition and dementia using several different continuous measures [14].

Although much is known about the effects of PD on the motor system, less is known about the link between PD, cognitive impairment and the resultant development of dementia [14]. Currently the motor symptoms of PD are treated with pharmaceuticals primarily L-DOPA (levodopa), the direct biological precursor to dopamine, which can cross the blood brain barrier where it is then converted to dopamine locally [11]. This treatment is only effective in the early stages of the disease before the patient develops a tolerance and only replaces the lack of dopamine partially relieving the motor and some non-motor symptoms of the disease [11]. Levodopa does not relieve or prevent dementia and it does not prevent the loss of dopaminergic neurons in the SNc [11]. No

curative treatment exists for cognitive impairment or dementia and the patients themselves have confirmed that cognitive deficiency is their primary concern with PD not the motor symptoms [16]. PDD is now the primary cause of disability, caregiver burden, healthcare expenditure and mortality due to PD [16]. A recent report from the Ministry of Health stressed the importance of improving care for dementia,

"*Dementia has risen to become the fifth-ranked cause of health loss in females and thirteenth in males. Providing better care for people living with mental illness, addiction and dementia – including care for their physical health – is a growing challenge for the health and social sectors."* [5]

80% of PD patients will develop PDD at some stage of the disease's progression as a direct result of PD itself, although the time at which a patient with PD transitions to PDD is highly variable and there is currently no method to predict exactly who will make the transition and when [16]. 25-62% of PD-MCI patients are at increased risk of developing dementia within 3 years, but not all PD-MCI patients are at imminent risk of dementia. This is important because the treatments and management of PD-MCI and PDD are different [17]. It is proposed that levodopa contributes to the decline in cognition and wouldn't be prescribed to PDD patients, however taking a PD-MCI patient off levodopa for the fear that they are at risk of developing dementia when they possibly won't would be inhumane [17]. In the future it may possible to treat dementia or slow its progression by introducing therapies prior to the decline from MCI to PDD. If some kind of intervention or therapy is to be developed to treat dementia one must be able to reliably predict who will make the transformation and when otherwise it is impossible to know whether the therapy staved off the dementia or whether the individual was never going to develop dementia in the first place. Several imaging techniques, diagnostic tests and clinical trials have been proposed to form a prognosis for transformation from PD-MCI to PDD by Melzer et al [18, 19, 20].

1.04 Clinical Examinations Used in the Diagnosis of PD, PD-MCI and PDD

There are several clinical examinations performed by clinicians to determine the current state of PD and its severity [14]. Each trial involves the patient performing a series of tests that are individually scored by the clinician and are often combined to form an overall continuous score that reflects the magnitude of severity of a particular aspect, or group of aspects, of PD [14]. These are performed to track the progression of disease somewhat quantitatively and to evaluate the potential benefits of therapy [14].

The Hoehn and Yahr scale is one measure of PD severity and is measured on a scale of 1 to 5. A patient score depends on specific states of physical independence and observation.

The Unified Parkinson's Disease Rating Score (UPDRS) is the most commonly used continuous scale in the clinical study of PD [21]. UPDRS is split into 6 separate parts with part II and III being used in this study. Each part is further broken down into subscales [21]. Part II is based on the patient's own self-evaluation of how PD is affecting their daily lives and capabilities [21]. Examples of subscales include grading their ability to walk, to keep from falling or turning in bed, to speak, to swallow and prepare their own food, get dressed, practise basic hygiene and to write [21]. Part III is a scored evaluation by a clinician of motor function based on physical measurements of individual patient performance [21].

Although UPDRS is the most commonly used scale for PD it has its limitations, including a lack of consistency among the scoring of subscales, the lack of reproducibility of subscales and primarily the small emphasis on non-motor features including cognition [21]. Criteria now exist for the diagnosis of PD-MCI developed by The Movement Disorder Society Task Force (MDSTF) specific to cognition designed to differentiate between PD-N, PD-MCI and PDD [14, 22]. Level II MDSTF criteria is made up of five cognitive domains, attention and working memory, executive function, language, learning and memory, and visuospatial performance [14]. Each domain is split into a series of tests with the results of each test given in terms of a z-score, which is the number of standard deviations of the result from the mean result accounting for age, education, and sex. PD-MCI is defined as a z score of -1.5 or 1.5 standard deviations below the average result in at least two tests within a single domain, PDD as having a z-score of -2 in any test within two domains and PD-N is defined as any patient that does not meet the criteria for PD-MCI or PDD [22]. The average z-score of all 5 domains can be used to represent the overall cognitive ability of the patient and is referred to as the cognitive z-score (CogZ).

1.05 Introduction to Quantitative Susceptibility Mapping and Magnetic Susceptibility

Quantitative susceptibility mapping (QSM) is a novel magnetic resonance imaging (MRI) post-processing procedure. Essentially QSM solves for the magnetic susceptibility of each voxel (3D pixel) in a multi-slice gradient echo (GRE) scan, in this case a brain scan, to give an idea of how the magnetic susceptibility varies in 3D throughout the brain [23]. Magnetic susceptibility, χ, is defined as the degree of magnetisation of a material (δM) subject to a unit magnetic field (δH) and is an intrinsic property of all materials [23],

$$\chi = \frac{\delta M}{\delta H} \quad \frac{Am^{-1}}{Am^{-1}} \tag{1.01}$$

M and H are both magnetic fields with the unit ampere per metre hence χ is dimensionless [23]. Magnetic susceptibility varies depending on the chemical constituents of the material and their bonding type and can either be positive (magnetisation parallel with the external field or paramagnetic) or negative (magnetisation anti-parallel with the field or diamagnetic) [23]. Therefore χ is a complex value with both magnitude and direction [23]. This property of χ causes the observed χ value to vary depending on the shape and orientation of the object being investigated relative to the externally applied magnetic field [23].

Iron is ferromagnetic and has one of the highest magnetic susceptibilities of any element, 200,000 (SI units); even in salt solution it has a χ, 0.00075 SI units, that is roughly 2 orders of magnitude higher than human soft tissue, -0.000009 (SI units) [23, 24]. Therefore with QSM small iron deposits in the BG and related structures could act as a non-invasive biomarker for PD and could show contrast with healthy individuals. If a correlation between QSM and PD is found in brain structures related to PD it may aid in the diagnosis of PD-MCI and PDD and more importantly the prognosis of PDD also.

1.06 Fundamental Physics of MRI

In order to understand the fundamentals of MRI you have to go right down to the building blocks of atoms. Wolfgang Pauli discovered in 1927 that subatomic particles such as protons, neutrons and electrons don't actually just sit still in their respective places in an atom, they actually rotate [25]. He also found that the same subatomic particles 'pair up' and spin in opposite directions to each other, effectively cancelling out each other's 'spin' [25]. If an element or isotope has an odd number of nucleons (protons and neutrons) then there will always be one un-paired nucleon [25]. This will give the nucleus a net spin (nuclear spin) [25]. All types of MRI rely on the property of nuclear spin [26]. Nuclear spin is possessed by the following atoms/isotopes, which are present in some amount in biological organisms0, ^{1H}, ^{2}H, ^{13}C, ^{14}N, ^{15}N, ^{17}O, ^{19}F, ^{23}Na and ^{31}P. ^{1}H and ^{13}C are the most common [25]. Nuclear spin is the net quantized or discrete intrinsic angular momentum of the above nuclei [25]. Nucleons do not

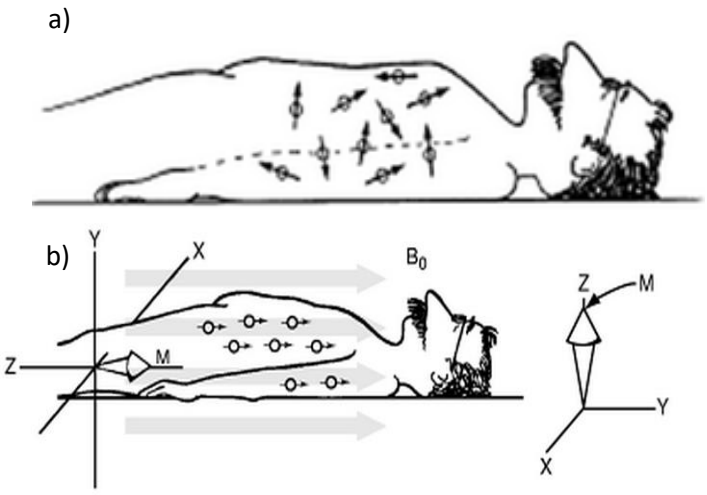

Figure 1.02 a & b: The alignment of magnetic dipoles in a human a) before an external magnetic field is applied and b) after an external magnetic field is applied [27].

have a continuous spectrum of angular momentums [25]. The spinning nucleon creates a magnetic dipole moment that points along the axis of rotation and this is proportional to its angular momentum [25]. Since angular momentum is quantized or fixed so is the magnitude of the magnetic dipole [25]. The Gyromagnetic ratio, γ, is equal to the ratio of the magnetic dipole to the angular momentum for a given element [25].

Nuclei naturally have their dipoles facing in all different directions (fig. 1.02a) [26]. When placed in an external magnetic field the majority of nuclei will align their magnetic dipoles parallel to the external field (fig. 1.02b) [25, 26]. This occurs because this direction is at the lowest possible energy state for the nuclei and like most chemical or physical processes in nature, a spontaneous move towards the lowest energy state usually occurs [26, 27]. This state is termed the ground state. Once the ground state is reached the net alignment of spins results in a weak magnetisation called longitudinal magnetisation, M_z, which is proportional to and in the direction of B_o, in the z-axis [26, 27]. A very small number of nuclei will actually align their dipoles antiparallel to the external magnetic field, but will require energy to do so as this is the highest energy state [26, 27].

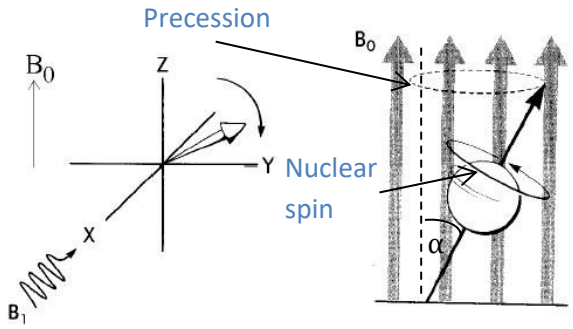

Figure 1.03: Rotation of net magnetisation due to an RF pulse, B_1, and nuclear precession about external magnetic field, B_o. The flip angle α is also shown [27].

Having aligned all the nuclei using a magnetic field, these nuclei can be excited using electromagnetic (EM) radiation such as a radiofrequency (RF) pulse, which is made up of an oscillating magnetic field, B_1, emitted for a fixed period of time [27]. This wave is emitted at an angle to the external magnetic field, B_o, and exerts a torque on the nuclei, consequently tilting the magnetisation into the transverse plane or x-y plane by a certain flip angle, α (fig. 1.03) [27]. This torque will cause precession, which is a complex repeated motion caused by tilting the axis of rotation of a spinning object and can be observed in spinning tops [25]. Precession occurs precisely at the Larmor frequency and is defined by,

$$\omega_o = \gamma B_o \qquad (1.02)$$

Where ω_o is the Larmor frequency (radians per second), γ is the Gyromagnetic ratio (Hertz per Tesla) and B_o (Tesla) is equal to the external magnetic field [25, 26, 27]. The excitatory RF pulse is chosen to be at the Larmor frequency so as to cause a torque on the nuclei [26, 27]. The α of the resultant torque is given by,

$$\alpha = \gamma B_1 \tau \qquad (1.03)$$

where γ is the gyromagnetic ratio, B_1 is the root mean square magnetisation of the excitatory pulse and τ is the time that the pulse is applied for [27]. The reason why a RF pulse is used is because the gyromagnetic ratio is fixed for a given atom and there are limits to how big the static magnetic field can be that is produced by the main coils in an MRI scanner. The main constituent of living organisms that has spin is hydrogen, which has $\frac{\gamma}{2\pi}$ = 42.58 x 10^6 Hz T^{-1} [25]. The highest magnetic field produced by a clinical MRI scanner is 7T, so the resultant Larmor frequency would be 42.58 x 10^6 x 7 = 298.06 MHz. This frequency just so happens to correspond with the part of the EM spectrum called radio waves. It also just so happens that RF waves can pass through organic matter relatively easily, which is ideal if we would like to image living organisms using this phenomenon [26].

Once the RF pulse ceases the nuclei will precess back toward the ground state, but since the nuclei have been displaced from their ground state they have gained energy [26, 27]. As the nuclei precess back toward the ground state this energy is released in the form of EM radiation also at the Larmor frequency [26, 27]. The transverse component of the radiation can be detected by receive coils as a changing flux as governed by Faraday's law [28]. The resultant EM radiation detected is a sum of all the individual fields from the precessing nuclei [28]. This process only works because the nuclei were prealigned prior to excitation [28]. Initially after excitation the nuclei all precess at the same time and consequently their magnetic fields all point in the same direction and add together [28]. If a RF pulse is emitted without an external magnetic field applied there is no incentive for the now excited nuclei to change direction or energy and any EM radiation produced is emitted in all directions effectively cancelling out [28].

The EM radiation detected by the receive coils can be used to construct an image, but in order to understand how to reconstruct an image from this signal, comprehension of the signal itself is required. The signal amplitude is proportional to proton density and also depends on two separate exponential relaxation processes, longitudinal or spin-lattice relaxation and transverse or spin-spin relaxation with respective time constants T_1 and T_2 [26].

When a body is first placed in the static magnetic field, B_o, the nuclei align to give a net longitudinal magnetisation of magnitude M_o [25, 26, 27]. If a RF pulse at the Larmor frequency is applied 90º relative to the external field then all of the longitudinal or z-component of the ground state magnetisation will be transferred to the transverse or x-y plane (fig. 1.04) [26, 27]. At the moment the RF pulse ceases the longitudinal magnetisation will be 0, but as the nuclei precess

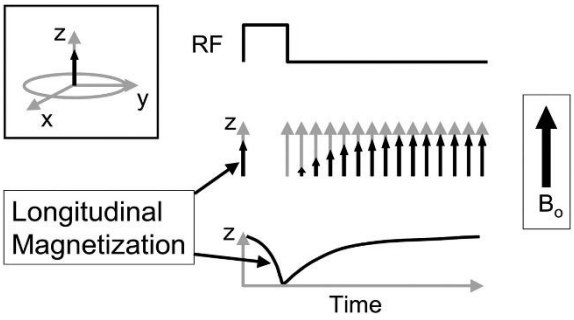

Figure 1.04: The exponential build-up curve for the magnetisation of nuclei in the longitudinal or z direction during and after a 90° RF pulse has been applied [29].

towards ground state this magnetisation in the longitudinal direction will increase [26, 27]. This is depicted by fig. 1.04 and the process can be described mathematically by the following equation, where t is the time elapsed after the RF pulse has ceased and T_1 is the time taken for the longitudinal magnetisation, M_z, to reach $M_o(1 - \frac{1}{e})$ or 0.632 of its maximum value, M_o [26],

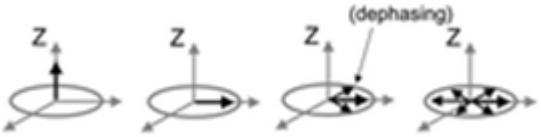

Figure 1.05: Going from left to right you have the initial magnetisation, M_o, then the RF pulse is applied tipping this magnetisation into the transverse plane, followed by dephasing, which is caused by variations in Larmor frequency for individual protons [27].

At the moment the RF pulse ceases the transverse magnetisation, M_{xy}, will be equal to M_o and will decrease as the nuclei return to ground state [26, 27]. It is often mistaken that the M_{xy} is being converted to the M_z during the return to ground state, but this is not the case as the two processes are independent of each other. The decay of the M_{xy} occurs faster than the build-up of M_z, i.e. $T_2 < T_1$ [26, 27]. This is due to an additional effect that reduces the M_{xy} called dephasing, which is demonstrated in fig. 1.05.

Each proton has a unique local magnetic field that it experiences determined by its specific location relative to other spinning nuclei nearby, which adds or subtracts from B_o to determine its individual precession frequency [26, 27]. Also slight variations in the static magnetic field depending on spatial location cause the precession frequency of protons to vary based on their position in the B_0 field. After an RF pulse the nuclei initially precess totally in sync or in phase, but as they precess towards the ground state they become gradually out of phase due to the slight variations in precession frequency caused by different magnetic field environments experienced by individual nuclei [26, 27]. This loss of coherence reduces the overall magnitude of the M_{xy}, which is termed dephasing [26, 27]. For a 90º pulse this dephasing does not affect M_z, as all the individual magnetic dipoles of nuclei always have a vertical component that is greater than or equal to zero, facing upward & parallel to the longitudinal direction, regardless of their relative phase [26, 27].

The M_{xy} does not show a simple exponential decay trend, but instead forms a simple harmonic motion like exponential envelope, which oscillates between positive and negative magnetisations

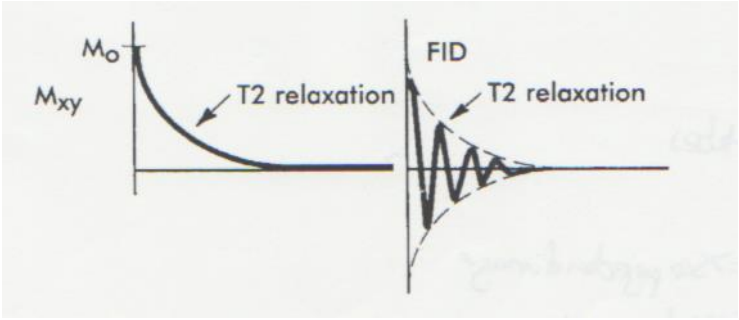

Figure 1.06: On the right is the damped simple harmonic motion (Free induction Decay or FID) of the transverse magnetisation, of which the amplitude decreases exponentially. The envelope of this oscillation indicated as the dashed line is plotted on the left and can be used to find T_2^* [27].

whilst decaying (fig.1.06) [27]. This is because precession is causing the magnetisation to rotate between a positive x-y transverse direction and a negative transverse x-y direction, changing the magnitude and sign of the transverse magnetisation continuously [27]. The envelope of the transverse magnetisation is usually all that we are interested in and this can be expressed mathematically as,

$$M_{xy} = M_{xyo}\, e^{\frac{-t}{T_2^*}} \qquad (1.04)$$

Note that T_2 *, not T_2 is used, which is the combined transverse relaxation constant,

$$\frac{1}{T_2^*} = \frac{1}{T_2} + \frac{\gamma \Delta B_o}{2} \qquad (1.05)$$

T_2* factors in the additional, recoverable de-phasing due to macroscopic magnetic field inhomogeneities ($\frac{\gamma \Delta B_o}{2}$) as well as pure T_2 non-recoverable dephasing due to inter and intramolecular interactions and magnetic shielding [30]. T_2* in equation 1.05 represents the time taken for the transverse magnetisation to fall to $\frac{1}{e}$ or 0.368 of M_o.

As discussed earlier T_1 is larger than T_2, with typical values for each time constant of 800ms and 30ms respectively [30]. However T_1, or T_2, or sometimes both T_1 and T_2, have different values in different tissues and this is a key property when looking at imaging an organism, as it allows us to differentiate between, and therefore potentially see, different tissue types in an organism [30]. In general, more dense tissues attenuate the transverse magnetisation faster, causing a reduction in T_2 and a faster transition to ground state so often T_1 is also reduced, so more dense tissues have lower T_1 and T_2 values [30].

If you want to form a multi-dimensional image, the precessing frequency of individual nuclei must be made dependent on its unique spatial position [30]. So far signals investigated are from samples placed only in a static magnetic field and are a measure of M_{xy} and M_z as a function of time with no spatial information [30]. Lauterbur introduced the concept of magnetic gradients

which are additional weaker magnetic fields with varying strength along a single axis for example the z-axis, mathematically expressed as [30],

$$G_z = \frac{\partial Bz}{\partial z} \qquad (1.06)$$

As seen in equation 1.02, protons precess at a Larmor frequency proportional to its local magnetic field strength and only transmit a signal when this matches the RF pulse frequency [25, 26, 27]. The total magnetic strength and resonating frequency as functions along this axis are therefore [30],

$$B(z)=B_o+z.G_z \qquad (1.07)$$

$$f(z) = \gamma(B_o+z.G_z) \qquad (1.08)$$

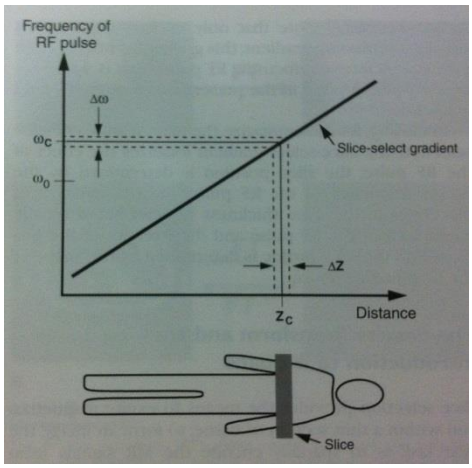

Figure 1.07: A linear magnetic gradient is applied on top of the static magnetic field giving each 'slice' of the subject its own unique Larmor frequency, ω_c. This can be used to select a slice, z_c by applying a RF pulse with a frequency equal to ω_c [30].

When magnetic gradients are applied, the detected signal which is an echo, has an intensity which is both a function of time and the magnitude of the chosen gradient [30]. Gradients can be applied along the three MRI axes, called slice select, readout (frequency encode) and phase encode, to allow unique intensity values for each spatial location enabling multi-dimensional imaging [30].

Firstly, a slice of tissue of arbitrary thickness, orientation and position is isolated by applying a magnetic gradient, G_S, in the slice select or z-axis, simultaneously with the RF pulse, as seen in fig. 1.07 [30]. The RF pulse applied does not have a single frequency, but rather a range of frequencies termed its bandwidth, and this determines slice thickness [30]. This slice is then spatially encoded in the remaining readout (x-axis) and phase encode (y-axis) directions.

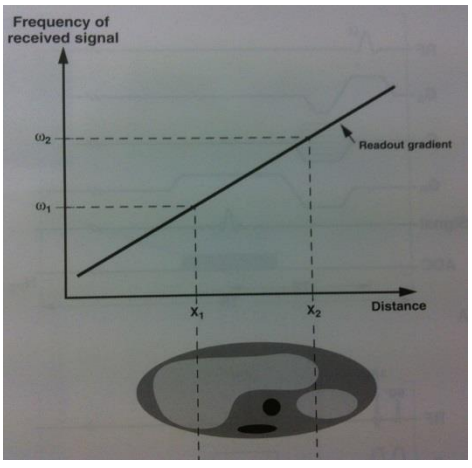

Figure 1.08: In the x plane of the slice selected in fig. 1.07 another magnetic gradient, G_f, is applied during readout of the emitted EM radiation from NMR giving frequency encoding of any given position along the x-axis [30]

The frequency encoding is described in fig. 1.08 and uses a second magnetic gradient, G_f, in the x-axis, which is applied during signal acquisition [30]. The phase encoding gradient, G_P, is applied between the RF pulse and the echo

signal and alters the phase of the nuclei prior to sampling the echo intensity [30]. Before G_P application protons are in phase, G_P however changes their precession frequencies according to position along the phase-encode axis, making them out of phase [30]. When G_P, is switched off, nuclei revert to the original frequency, but are now phase encoded as they keep these acquired phase angles (fig. 1.09) [30]. Therefore by using G_S, G_f and G_P one can isolate an MR signal from a single voxel in 3D space. The various unique combinations of RF, G_S, G_f and G_P gradient pulses with respect to time are called pulse sequences [30].

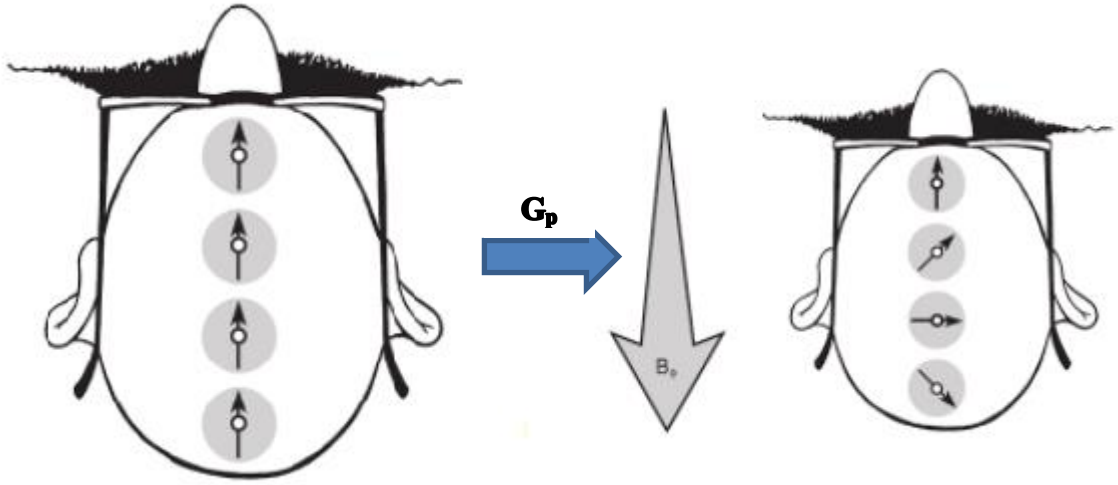

Figure 1.09: Demonstration of phase encoding. B_p is the direction of the magnetic field due to the phase encode gradient G_p. The gradient causes a fixed spatially dependent phase difference between spins in the direction of the phase encode gradient [27].

In order to produce an image however you require an echo. An echo can be created by inverting the proton spins with a 180˚ RF pulse [27]. This takes the protons that have a higher Larmor frequency that were leading in terms of phase (fig. 1.10b) and causes them to lag (fig.1.10d), and the protons with a slower Larmor frequency that were previously lagging behind now lead in terms of phase [27]. The protons with a higher Larmor frequency catch up to those with a lower Larmor frequency causing a regaining of

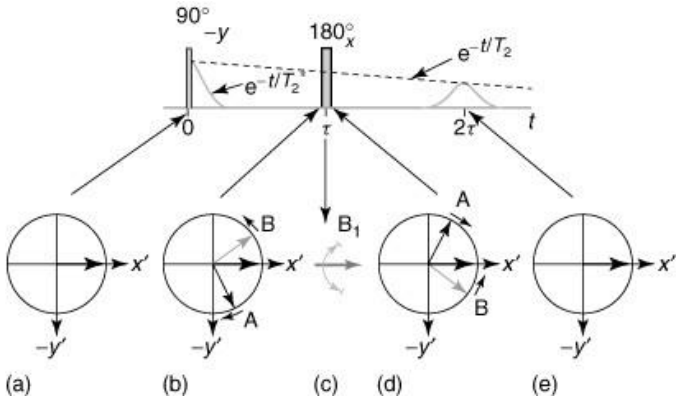

Figure 1.10: An example of the basic spin echo pulse sequence accompanied by the equivalent magnetization vectors at key stages of the sequence. a) 90º RF excitation pulse is applied tipping M_z into the transverse plane. b) dephasing occurs with leading (A) and lagging (B) vectors cancelling out and reducing observed M_{xy} signal. c) 180 º RF pulse inverts the spins. d) the once leading A now lags in phase, but due to its higher Larmor frequency it begins to catch B. e) A catches up to B or refocuses leading to an echo [31]. The echo occurs at 2τ where τ is the time between the excitation pulse and the 180˚ pulse, which allows one to know exactly when to read in the data [27].

phase coherence and a secondary peak in signal amplitude called an echo (fig.1.10e). This is what is individually measured in every voxel of an MRI image [27]. The echo occurs at exactly 2τ where τ is the time between the excitation pulse and the 180˚ pulse, which allows predictable measurement of the echo signal [27]. MRI that uses a 180˚ RF pulse to create an echo is called spin echo imaging [27].

Another method that can be used to generate echoes uses gradients to refocus the proton spins instead of a 180° RF pulse [27]. Spins are dephased by a successive series of pulsed gradients in the phase encode axis with a gradual reduction in amplitude of each pulse before spins are rephased by a series of pulsed gradients with the exact opposite polarity and amplitude to generate the echo [27]. This method of MRI imaging is called gradient echo (GRE). GRE differs from standard spin-echo in that it can only be weighted to T_2^* and it allows the use of flip angles less than 90°, which also shortens imaging time [27]. If GRE is coupled with a spoiler gradient which destroys residual signal left over after an echo has been read, then one can image very rapidly [27]. This method of imaging is called spoiled gradient echo (SPGRE) [27].

The resultant magnitude of the signal that is produced as a result of the echo is dependent on its relaxation parameters T_1, T_2 or T_2^*, the time between excitation RF pulses or the repetition time (TR) and the amount of time between the excitation RF pulse and the generated echo or the echo time (TE) [27]. By changing TE and TR parameters one can 'weight' the image for T_1 or T_2 [27]. You will see contrast in your resultant image between tissues of varying T_1 or T_2 depending on which relaxation process you applied weighting to [27]. In general short TRs give little time for M_z to recover before the next excitation and hence tissues with a long T_1 appear dark and tissues with a short T_1appear dark and tissues with a short T_1 appear bright giving T_1 weighting (fig. 1.11a)

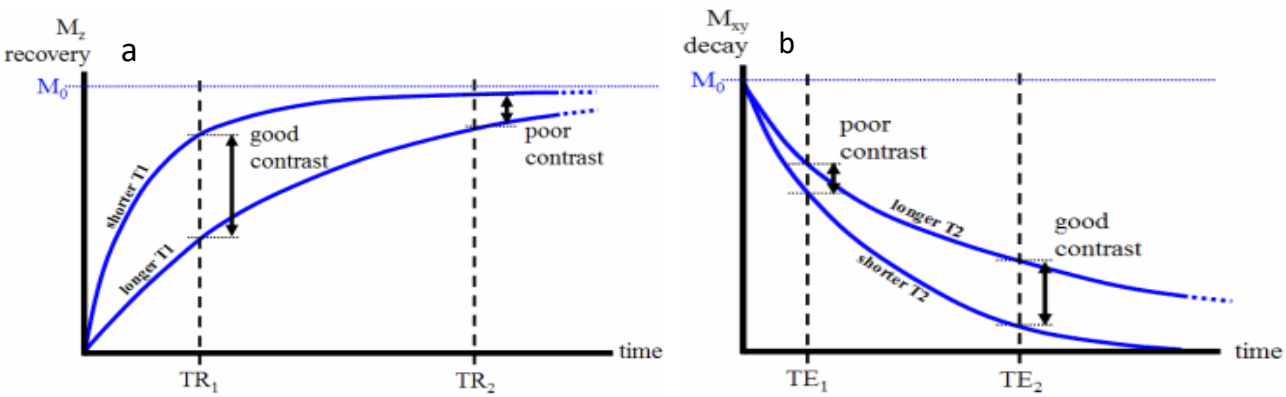

Figure 1.11a & b: a) Longitudinal relaxation of materials with different T_1 values after a standard 90° RF pulse. Suggested times, TR1 and TR2 for a possible second RF pulse that can be used to generate contrast in a T_1W image are included [34]. b) Transverse relaxation of materials with different T_2 values after a standard 90° excitation. Included are suggested times, TE1 and TE2, to measure an echo and generate contrast in a T_2W image [34].

[27]. Long TEs allow tissues with a short T_2 to decay completely whilst tissues with a longer T_2 retain signal providing T_2 weighting (fig. 1.11b). Different tissues in the human body have different spin lattice arrangements and hence different T_1s therefore T_1 weighted imaging is commonly referred to as structural imaging and is used to obtain detailed structural and anatomical information [27]. Pure T_2 imaging is used less often however T_2* weighted imaging follows the same lines as T_2 and is used in a variety of applications, from functional MRI to diffusion MRI [27].

Signals are measured in receive coils via EM induction perpendicular to the B_0 field and can only be measured in the transverse plane due to requiring Faraday's law to be detected [27]. When signals are detected they are not detected as one, but rather a pair of x and y components in the transverse plane separated by 90 degrees (fig. 1.12) [27]. These are referred to as real (x) and imaginary (y) components [27]. For typical gradient echo MRI real and imaginary data are acquired for each voxel in the image [27]. The real and imaginary components are then usually combined together to form either a magnitude or a phase image and afterward the raw real and imaginary components are discarded [27].

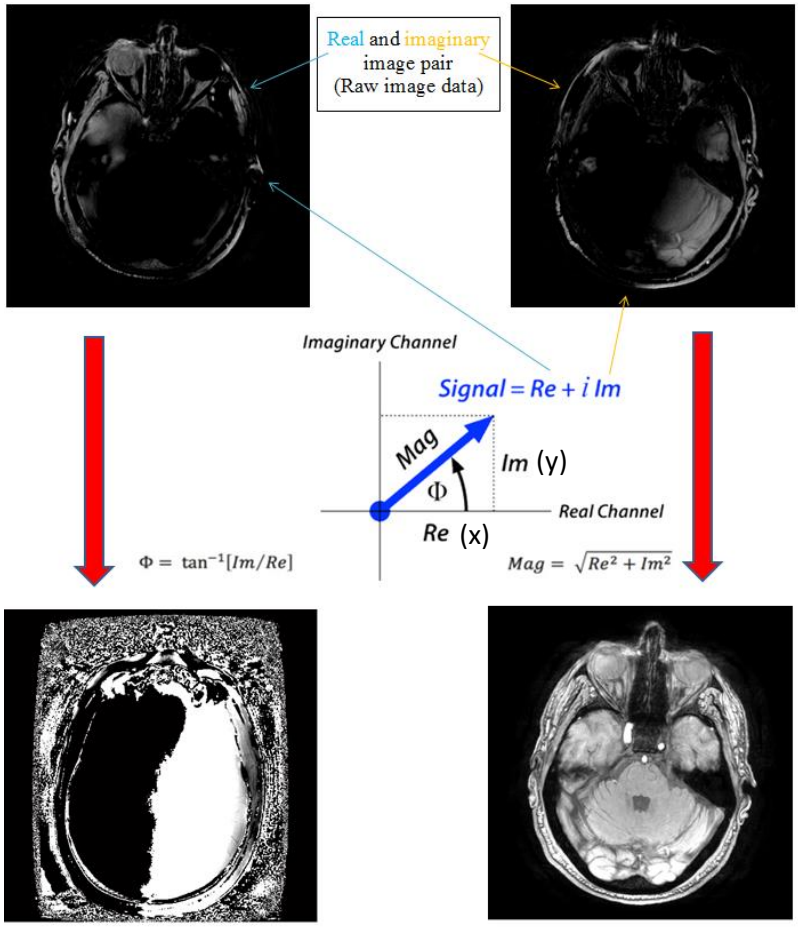

Figure 1.12: Demonstration of how to make a phase image and magnitude image from raw real and imaginary images [32]. The phase image on the left is given as the arc tangent of the imaginary image divided by the real image. The magnitude image is given as the square root of the sum of squares of the real and imaginary images [32]. Images obtained from the New Zealand Brain Research institute (NZBRI).

1.07 Image Acquisition & Fundamental Physics of Quantitative Susceptibility Mapping

SPGRE is the most commonly used sequence for QSM [23]. The first major point of difference between standard SPGRE MRI and that used for QSM is that we actually instruct the machine to

store the data as a real and imaginary image pair instead of a magnitude or a phase image [23]. This is because we need to be able to generate both of these images to perform QSM [23].

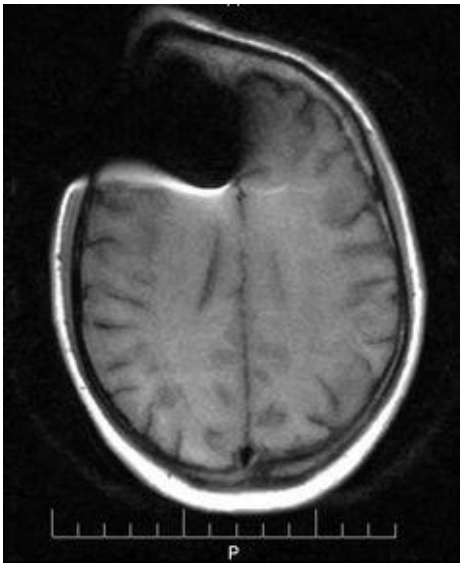

Figure 1.13: Demonstration of the magnetic susceptibility artefact. Susceptibility artefacts of this magnitude are often caused by a hairclip or other metallic object located in the imaging volume. The local field generated by the object with high magnetic susceptibility is large enough to shift the Larmor frequency and phase so that the signal is accidentally taken as coming from a different spatial position in the image (anatomical warping) or large enough to not even be selected (signal loss) [33].

The basis of QSM actually stems from an artefact seen primarily in GRE imaging called the magnetic susceptibility artefact [23]. When the main B_0 magnetic field is applied to a person during MRI that person responds by becoming magnetized [23]. If there is a difference in magnetisation between voxels, as is the case with most tissue interfaces or boundaries, this will produce a much smaller local magnetic field that alters the Larmor frequency and hence the phase of the precessing protons from what they're expected to be, similar to the phase encode gradient explained in section 1.05 [23, 27]. The larger the difference in magnetic susceptibility the larger the local magnetic field is and the larger the frequency and phase shifts [23]. Most tissues in the human body don't have very high magnetic susceptibilities so these local fields are typically small enough to be ignored [23]. They only become a problem when objects of high magnetic susceptibility, like metal implants for example, are in or near your image volume (fig. 1.13) where they can cause anatomical warping and significant loss of signal [23]. The phase and frequency shifts are time dependent so with longer echo times you can still experience some small signal loss and spatial warping as a result of less significant magnetic susceptibility differences such as those seen in the human body [23]. Magnetic susceptibility differences also lead to an artefact whereby objects with higher magnetic susceptibilities appear larger in the image then their true size and this is called partial voluming [23]. Since GRE is T_2* weighted it is particularly sensitive to the magnetic susceptibility artefact as the most significant contributor of field inhomogeneities causing T_2* decay are tissue boundaries and susceptibility differences [23]. For the above reasons longer TEs are generally avoided in standard GRE [23].

Instead of suppressing or avoiding the magnetic susceptibility artefact, QSM actually uses it to obtain extra information about the tissues being imaged [23]. The goal of QSM is to purposefully exaggerate any natural magnetic susceptibility artefacts as much as we can by imaging with GRE over a prolonged TE, then measure the resultant phase shifts generated by local magnetic fields

by generating phase images and finally back calculate what the magnetic susceptibilities would have been that produced the observed local magnetic field [23, 35].

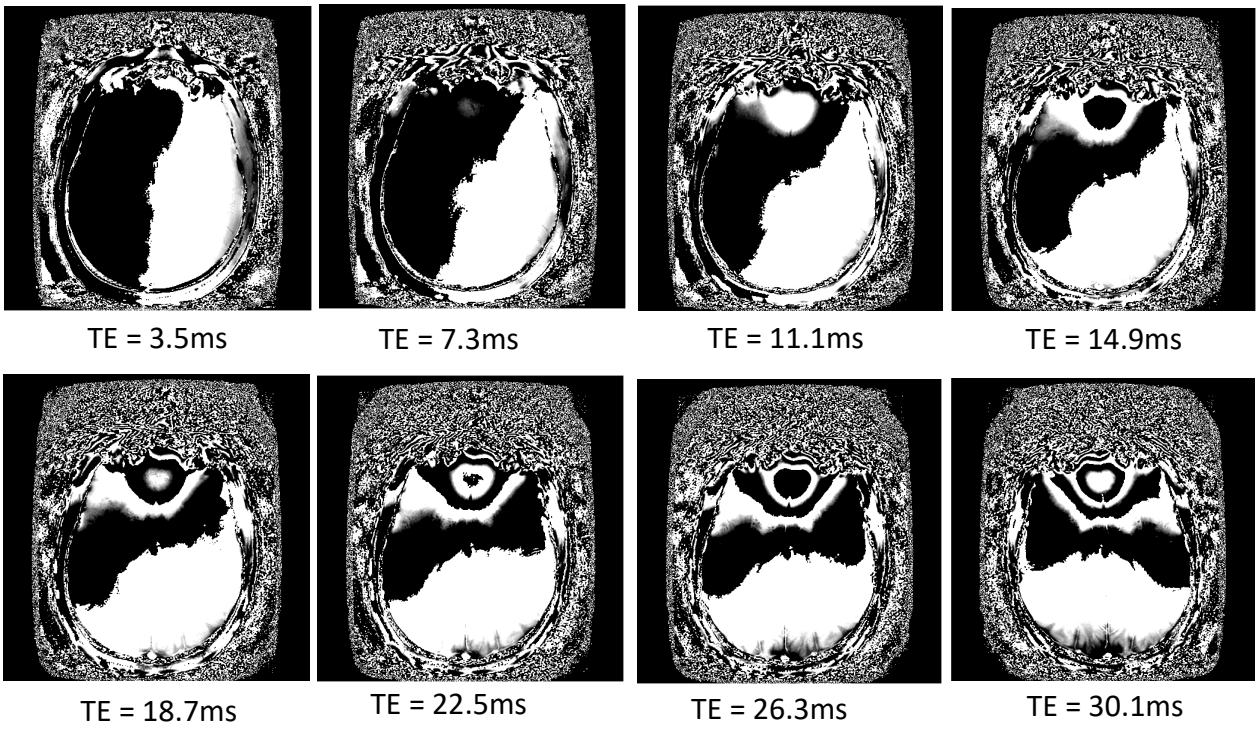

Figure 1.14: A series of 8 phase images taken with SPGRE at different echo times (TEs) ranging from 3.5 to 30.1ms. As time goes by the noise in the phase images gradually increases. Images obtained from the New Zealand Brain Research institute (NZBRI).

The first step toward QSM is working out the phase shift due to susceptibility differences, which is simply the difference between two successive phase images of the same slice. Since there are relatively small differences in magnetic susceptibility you have to image over a fairly long time to establish these small differences in susceptibility as detectable and distinct phase shifts [23]. The problem is as you image over a longer period of time the overall signal that the phase is extract from decays exponentially and eventually all that is left is noise (fig. 1.14) [27]. So instead of taking one image at say 3ms and another at 30ms, you take multiple images between 0ms and 30ms at regular time intervals and use them to get a better idea of what the total phase shift is without being significantly impacted by noise [35]. This method also improves the overall signal to noise ratio of the magnitude image used later in processing [35]. In order to perform this you need a very fast imaging sequence and hence SPGRE is the ideal sequence for QSM.

Ideally the observed phase shift (φ) is equal to the local change in magnetic field (δB) due to susceptibility divided by the gyromagnetic ratio (γ) multiplied by the echo time (TE) [36].

$$\varphi = -\frac{\delta B}{\gamma TE} \qquad (1.09)$$

This should give a straight forward linear relationship between the observed phase shifts obtained and $\frac{1}{TE}$ to yield the local magnetic field in each voxel, but unfortunately this formula does not hold due to the noise in the phase images. A better approach solves a nonlinear least squares problem in each voxel to account for the growing noise in each subsequent image [35]. Besides the non-linear model the curve is also weighted such that the first calculated phase shift, which has the least noise, has the highest weighting and the last phase shift has the lowest [35].

$$\delta B = argmin \sum_{j=1}^{N_e} \left| S(r, TE_j) - A(r, TE_j) e^{-i\phi(r)\omega_0 TE_j} \right|^2 \qquad (1.10)$$

Where $S(r, TE_j)$ is the total measured complex amplitude of the MRI signal (phase + magnitude) at position r in the image at the jth TE and $A(r, TE_j)$ is the modelled signal represented as a complex amplitude multiplied by a phase, ϕ, linear in time at the same r and TE with angular velocity ω_0 equal to the Larmor frequency (Eq. 1.02) [35]. After complex TE curve fitting of the raw image data to determine the local field, δB, it is possible for total phase shifts to occur that are greater than 2π causing these voxels to appear as if they haven't undergone any phase shift at all. Phase unwrapping is a process that corrects the local field for this effect by checking that the phase in the image is spatially continuous [35].

The difficulty in working out QSM is that the local magnetic field in any given voxel of the image isn't solely produced by the magnetic susceptibility differences between that voxel and its neighbouring voxels, it's also theoretically affected by every other surrounding voxel as well not just in 2D, but in 3D, all of which can have different unknown magnetic susceptibilities [36]. Each voxel effectively acts as an individual magnetic source with its strength directly proportional to χ and from the total combined field of these susceptibility sources we somehow have to determine each individual source's strength [36],

$$\delta B = B_0 (X \otimes d(r)) \qquad (1.11)$$

Where *X* is the magnetic susceptibility distribution of your image and *d(r)* is the magnetic dipole kernel given by the following expression [36],

$$d(r) = \frac{3\cos^2(\theta) - 1}{4\pi r} \qquad (1.12)$$

Where (θ) is the angle between the direction of B_0 and $d(r)$ [36].

This problem can be solved using spherical deconvolution and the problem is made much simpler due to the fact that the local fields produced within the human body are small and often only act

over distances of no more than 5mm, which is what is used as the radius of the spherical kernel [36].

The problem is however that there isn't just one, but in fact many different magnetic susceptibility distributions that can give rise to the exact same observed local magnetic field map, also known as an ill-posed problem [36]. There isn't actually enough information to narrow down the possibilities to a definitive answer. This is complicated further by noise in the phase images that derived the local field so one cannot be exactly sure what the actual local magnetic field really is [35]. So in order to quantify magnetic susceptibility in each voxel we have to pick one solution out of countless different possibilities that actually represents the true underlying tissue properties that we're interested in [36]. There are a few different ways to do this and there is still a bit of debate over which method is the best, however non-linear morphology based dipole inversion (MEDI) appears to have the best accuracy and reproducibility [35, 37].

MEDI uses a magnitude image from the raw real and imaginary data as an 'a priori' to find out as much as possible about the nature of the true χ distribution in order to make an informed decision on which solution to choose [36]. There are two specific pieces of information in the magnitude image that can be used. The first is the edges [36]. The edges give us a good idea of where the tissue boundaries or interfaces are in the image [36]. These are the areas that are most likely to experience the largest difference in magnetic susceptibility and the edges can be found within the magnitude image automatically using an edge filter [36]. The second piece of information that can be used is which areas are homogenous [36]. These are the areas that are most likely to have the same magnetic susceptibility [36]. The homogenous areas of an image can be obtained by subtracting the edge filtered image from the original magnitude image [36]. These two pieces of information are used to construct two separate matrices, each containing weightings representing the likelihood of any given voxel having a different magnetic susceptibility from its neighbours or the same magnetic susceptibility as its neighbour [36]. Then Bayesian regularization is performed minimizing the sum of squared differences between the local field generated by the proposed X and that of the local field distribution (δ), with these two matrices acting as additional constraints. The full minimization problem is given below:

$$min_X \|W(CX - \delta)\|_2^2 + \alpha^2 \|W_0 X\|_2^2 + \beta^2 \|W_1 X G\|_2^2 \qquad (1.12)$$

Where X is the magnetic susceptibility distribution, δ is the local magnetic field map, C is the convolution kernel matrix, α and β are regularization terms, W is a matrix containing weightings for the noise in δ, W_0 and W_1 are the homogeneity and edge matrices containing the weightings

for homogenous regions and edges respectively and G is a matrix containing the gradient operator along each axis of the image [36].

However the process described above has one major oversight and that is that you assume there is only small magnetic susceptibility differences and therefore only local fields present that act over small distances [35]. There is one tissue in the human body that does have a significantly higher susceptibility then most others and that tissue is bone, specifically the calcium in bone, and when the magnetic susceptibility artefact is purposefully exaggerated the skull to air and skull to dura interfaces produce a magnetic field large enough to actually cross over into the brain [35]. QSM can't be performed in the brain with this background field present so what needs to be done is not just determine the local field within the brain, but also determine the field generated outside the brain by the skull and air interfaces as well, using Maxwell's equations [35]. Then the background field is subtracted from within the brain mask prior to performing inversion.

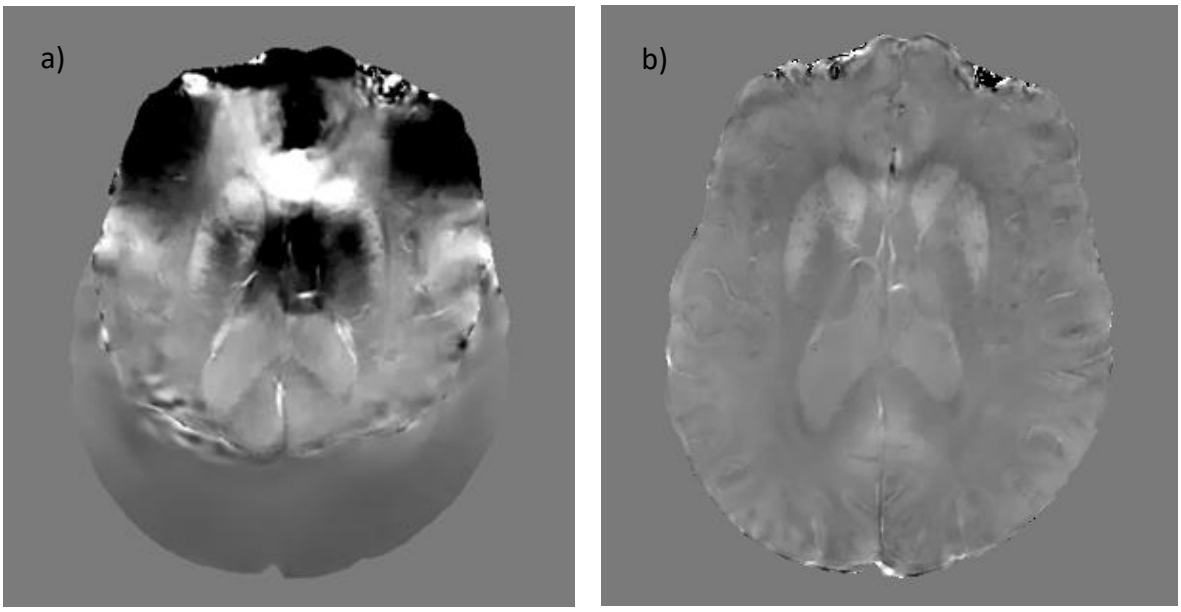

Figure 1.15a & 1.15b: a) a QSM reconstruction of the brain without background field removal (BFR) and b) a QSM reconstruction with Laplacian boundary value (LBV) BFR demonstrating the impact of the residual field generated by the skull. As can be seen in figure 1.14a artificial signal has drifted into the anterior and posterior regions of the brain [Liu2013]. Images obtained from the New Zealand Brain Research institute (NZBRI). The window and level of both images is 0.5 & -0.25 respectively.

Because there are tissues in the body that are diamagnetic and paramagnetic, both positive and negative values are naturally present in QSM images.

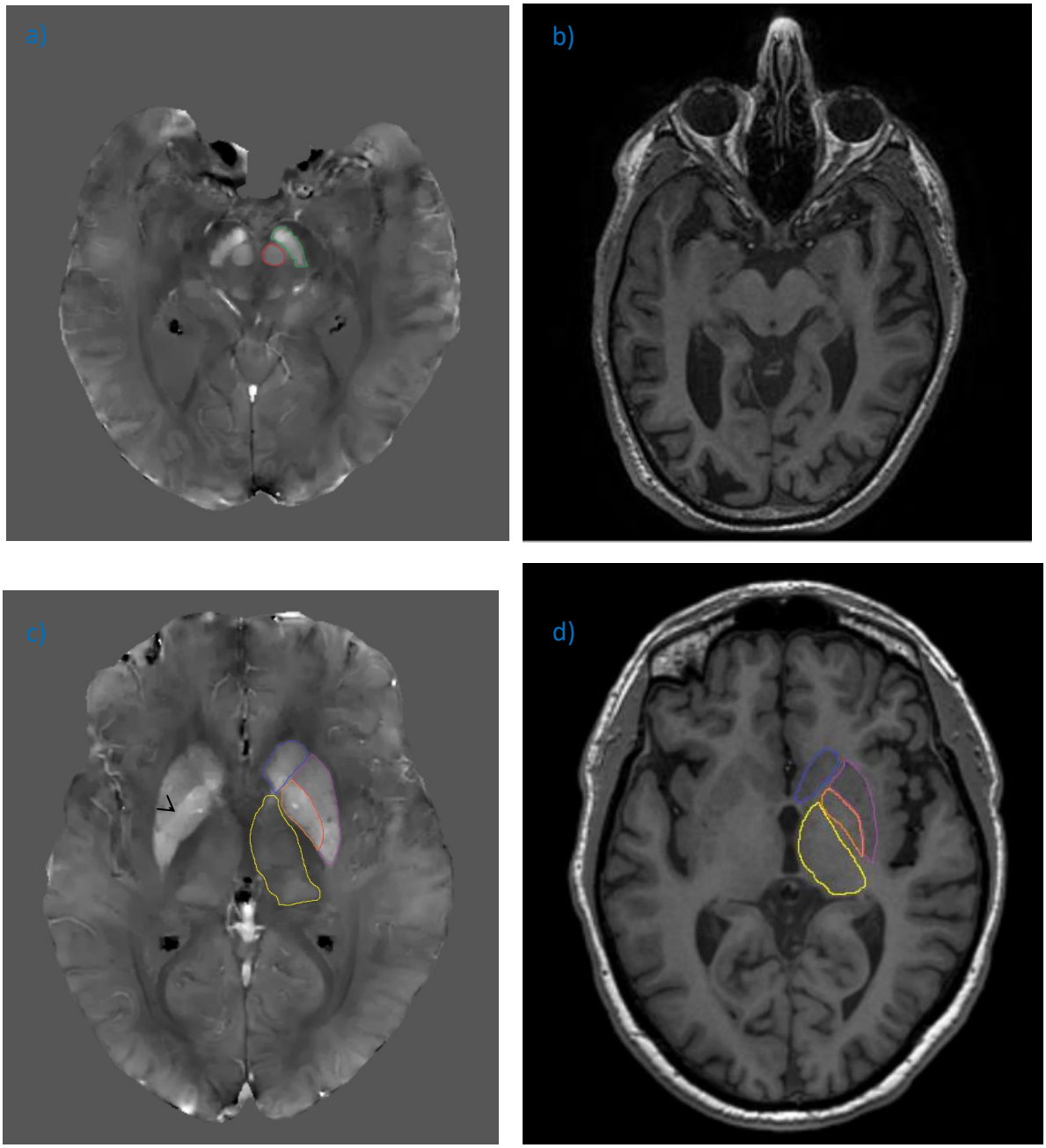

Figure 1.16a-d: Exemplar QSM images and comparison with structural T_1-weighted images. Figure 1.16a demonstrates two of the most prominent structures visible in QSM; the substantia nigra (green) and the red nucleus (red). These structures are near invisible in the structural T_1-weighted image (Figure 1.16b). Figure 1.16c & d demonstrate the globus pallidus (orange) and putamen (purple) collectively called the striatum, the caudate nucleus (blue) and the thalamus (yellow). QSM is capable of accurately depicting the medullary lamina that separates the internal and external segments of the globus pallidus as indicated by the black arrow. Note that the QSM BG structures appear larger than the true anatomical size of the structural T_1-weighted image demonstrating the extent of partial voluming. The QSM images have a window and level of 0.5 and -0.25 and the structural images have a window and level of 10,000 and 500. Images obtained from the New Zealand Brain Research institute (NZBRI).

QSM produces the highest known contrast and signal to noise ratio out of any other MRI sequence or virtually any other non-invasive imaging modality for that matter for several key grey matter structures in the brain [(36)]. Two very prominent examples are the SN and the red

nuclei (RN), which are near invisible in structural T1-weighted images, however in QSM they show up very clearly (fig. 1.16a) due to their naturally higher iron content. Another prominent example is the striatum in which you can clearly differentiate between the GP and the putamen (fig. 1.16c) and sometimes even between the internal and external segments of the GP. The caudate and thalamus are also often distinguishable.

1.08 Previous Studies on PD using QSM

Recent studies by Langkammer, Schweser and Zheng et al have estimated iron deposition in the brain non-invasively using QSM [38]. Barbosa, Guan, He and Du et al then correlated iron deposition in the SNc, estimated with QSM, to PD, however these studies did not investigate the links between iron accumulation in BG structures and cognitive impairment in PD or the development of dementia [38, 39, 40, 41]. Du et al also found that QSM in the SNc correlated with the duration of disease, with UPDRS II scores & Levodopa equivalent daily dosage. Guan et al noted patients with 'late PD' (Hoehn & Yahr >3), had additional increases in QSM in the SNr, GP (especially internal GP) and RN compared to early PD (Hoehn & Yahr<2.5) and HCs. Iron is used in neural metabolism throughout the brain not just in the SNc and other dopaminergic sites, hence it is possible that iron accumulation could occur in other nuclei associated with the SNc such as the SNr and GP as a result of PD [42]. The Hoehn & Yahr scale is primarily gauged on motor symptoms, which are primarily the cause of SNc degeneration, with the SNr and GP being involved in some cognitive [14]. It's possible that the increases in QSM Guan et al found in the SNr and GP interna weren't related to Hoehn & Yahr at all, but in fact were related to underlying cognitive decline, which is coincidentally more common in later stages of PD [16]. Guan however did not investigate whether these increases in QSM outside of the SNc were related to cognition. Acosta-Cabronero et al. performed the first whole brain QSM analysis in late 2016 noting no global differences in QSM for striatum or primary motor and somatosensory cortices, but differences in parts of temporal, paralimbic, occipto-parietal & prefrontal cortices as well as the rostral pontine area [42].

1.09 Project Aim

The first goal of this study was to demonstrate increased QSM values in the SN_c in PD relative to controls. The second goal and primary aim of this study was to determine whether increased QSM in the SN and associated nuclei is correlated with cognitive impairment in PD. A final aim was to perform a whole brain QSM analysis, as opposed to single grey matter structures, to test whether cortical QSM is (1) increased in PD, and (2) correlated with cognitive impairment.

Chapter 2: Method

2.1 Subjects, Clinical Assessment & Image Acquisition

A convenience sample of 114 participants meeting the UK Parkinson's Disease Society's criteria for idiopathic PD was recruited from the Movement Disorders Clinic at the Van der Veer Institute for Parkinson's and Brain Research, Christchurch, New Zealand. Volunteers representative of the broad spectrum of cognitive status in PD were invited to participate. The control group comprised of 30 healthy volunteers matched to the whole PD sample for mean age, years of education and sex ratio. Exclusion criteria included atypical parkinsonian disorder or other CNS disorder; previous history of other neurological conditions including moderate or severe head injury, stroke, learning disability or vascular dementia; and major medical illness in the previous 6 months. 15 subjects were excluded due to having insufficient or no clinical data. 6 more were excluded due to excessive motion artefacts (visually assessed) as motion arteficially induces phase shifts, leading to unreliable QSM values. 1 subject was excluded due to incorrect scanning parameters, and later 2 others due to processing errors. Analyses were conducted on the remaining 97 PD and 24 control subjects. This sample provides a reasonable representation of the local community of PD patients, including the full spectrum of cognitive impairments, as our Movement Disorders Clinic assesses the majority of patients in the region. All subjects gave written consent, with additional consent from a significant other when appropriate. The Upper South Regional Ethics Committee of the New Zealand Ministry of Health approved the study.

Disease severity was assessed using the Unified Parkinson's Disease Rating Scale (UPDRS: part III, motor). Comprehensive neuropsychological testing classified PD patients as either cognitively normal (PD-N; n=31), with mild cognitive impairment (PD-MCI; n=56) or with dementia (PD-D; n=10), using level II clinical criteria established by the Movement Disorders Society (MDS) Task Force as outlined by Wood et al. [(22)]. Dementia diagnosis was also based on the MDS Task Force criteria. PD-MCI cases had unimpaired functional activities of daily living, but scored 1.5 SDs or more below normative data on at least two measures within at least one of the four MDS Task Force cognitive domains (executive function; memory; attention, working memory and speed of processing; and visuospatial/visuoperceptual function).

The mean age for the entire study population was 72 years with a standard deviation of 7 years. Table 1 below summarizes the sex distribution across the different categories. The categories were evenly distributed between male and female except for PDD.

Sex	Healthy Control	PD-N	PD-MCI	PDD	Total
Female	6	11	16	0	33
Male	18	20	40	10	88

Table 2.1: Sex distribution of the population. The ratio between male and female is 8:3, which is normal, PD is more common in males than females. There was roughly an even distribution of sex in each category except PDD due to limited availability.

Image Acquisition: Real and imaginary image pairs were acquired for 8 different and evenly spaced TEs between 3.8ms and 32.1ms (3.8ms TE spacing) using a spoiled gradient recalled echo (SPGR) sequence with TR=42.8ms, flip angle=20° and a bandwidth of 244.141Hz. This was repeated for 60 transverse slices (2mm thickness) per subject covering the total volume of the brain. The QSM image matrix was 512x512 with a FOV=240mm resulting in 0.47mm x 0.47mm x 2mm voxels. Total scan time was ~5 minutes. Structural T_1-weighted images, with a TR= 6.6ms, TE=2.8ms, α=15°, a bandwidth of 122.07Hz an image matrix of 256 x 256 and voxel size 0.98mm x 0.98mm x 1mm (170 slices, total imaging time=5:09) have also been acquired separately for the purpose of caudate, GP, putamen and thalamus segmentation as structural T_1-weighted imaging has the highest resolution and contrast for these nuclei. All imaging was performed using a GE Healthcare Signa HDxt 3T MRI scanner at Hagley Radiology.

2.2 Pre-processing

Initially a check was done to ensure that the duration between each TE of each image for a given slice, or the TE spacing, in all subjects was held constant as the QSM code requires this to be constant and will otherwise interpolate phase to constant TE across all images introducing additional error [35]. The duration between each TE was found to be constant within all subjects with only two subjects showing a minor variation (3.812 & 3.848) in TE spacing compared to the other 110 subjects (3.808ms). All subjects also had minor variation in the first TE (±0.05ms). The overall standard deviation in each of the 8 TEs between subjects was found to be no more than ±0.06ms.

All the acquired images were converted from the DICOM format that they were initially obtained with to NIfTI using statistical parametric mapping (SPM) 12 software. NIfTI is a file format that allows us to perform several key steps in data processing and analysis such as coregistration and normalisation with SPM 12 and linear regression analysis with FSL, and is also part of the current convention for neuroimaging. Down sampling was performed on the structural T_1-weighted images due to the DICOM to NIfTI conversion producing unnecessary and excess interpolation also with SPM12.

2.3 QSM Testing & Reconstruction

In order to produce the quantitative susceptibility maps (QSMs) we used a MATLAB code provided by T. Liu et al (University of Cornell) [35]. The code produced QSMs using the following procedure [35, 36, 43, 44, 45]:

1. Importing the raw real and imaginary image data as a 4D file with echo time as the 4th dimension.
2. Generating magnitude images calculated as the following,

$$Mag = \sqrt{\frac{x_1{}^2 + y_1{}^2 + x_2{}^2 + y_2{}^2 + x_3{}^2 + y_3{}^2 + \cdots x_8{}^2 + y_8{}^2}{8}} \qquad (2.1)$$

   Where x_n and y_n represent the real and imaginary images.
3. Complex TE curve fitting of the raw SPGRE image data to estimate the local magnetic field
4. Region growth spatial phase unwrapping.
5. Background field removal (BFR) using either projection onto dipole fields (PDF) or Laplacian boundary value (LBV) methods.
6. Reconstruction of quantitative susceptibility maps using non-linear morphology enabled dipole inversion (MEDI) with a kernel radius of 5mm, regularization parameter, λ, of 1000, an edge parameter of 0.9 and a threshold of 0.1 with units of parts per million (ppm).

Prior to generating QS maps for the entire population, the non-linear MEDI QSM code was first tested to ensure that it was correctly producing QS maps. Firstly exemplar data provided with the code was successfully reconstructed. After fixing several issues with data importation and altering the code to use NIfTI instead of DICOM images, our own images were successfully reconstructed with the default BFR, projection onto dipole fields (PDF). It was then discovered that the inbuilt threshold based brain masking program was substandard and was erroneously including the eyes in the brain mask (fig.2.01a), which in turn introduced background field artefacts (fig. 2.01c). This default masking program was replaced with the FMRIB Software Library's (FSL's) brain extraction tool (BET) with fractional intensity thresholds (f) and vertical gradients in fractional intensity thresholds (g) that were tailored to each individual for the best possible brain masks (fig. 2.01b).

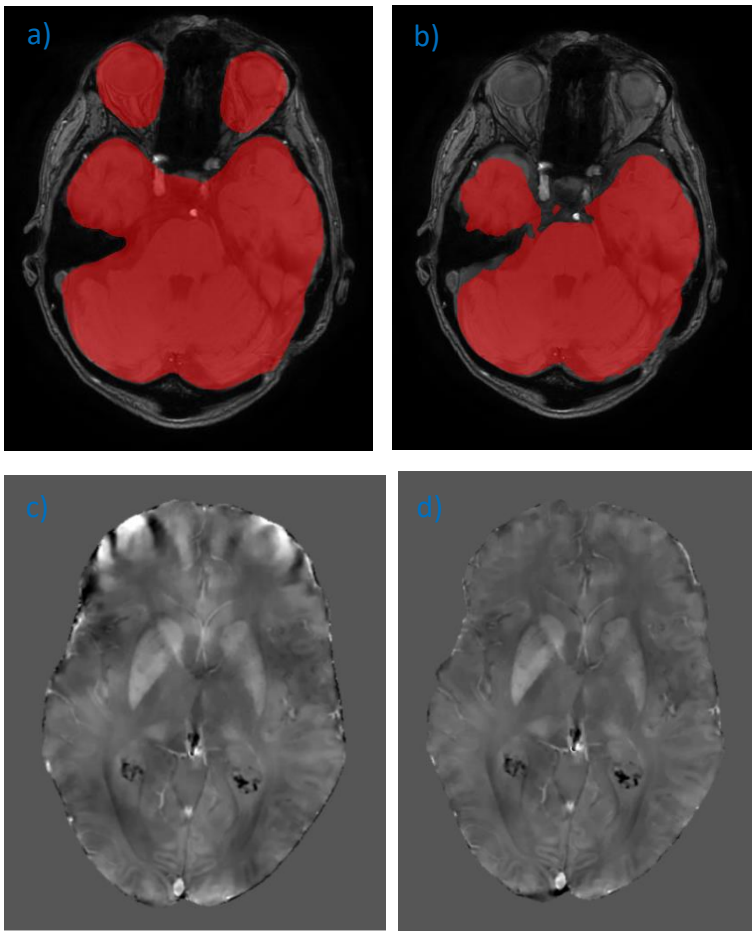

Figure 2.01a-d: Comparison of inbuilt threshold based masking (fig. 2.01a) to FSL BET masking (fig. 2.01b). a) and b) are magnitude images of the same slice with the masks overlaid onto them in red. c) and d) are the resultant QS maps reconstructed with PDF BFR. As you can see in fig.2.01a the eyes have been included in the threshold based mask and as a result the reconstructed QS map in fig. 2.01c contains unremoved residual background field. FSL BET masking shown in fig. 2.01b is much more accurate than the threshold based method and hence the reconstructed QS map with FSL BET, fig. 2.01d, does not contain the background field artefact from the eyes. The QSM images have a window and level of 0.5 and -0.25. Images were obtained from the New Zealand Brain Research institute (NZBRI).

Having successfully reconstructed QSM with the new masking, the different methods of BFR, PDF and solving a Laplacian boundary value (LBV) were tested. PDF was found to contain a background artefact, which was greatly reduced by LBV. Also 6 subjects with PDF BFR failed to reconstruct. Based on these observations and research conducted by Santin et al. who found that non-linear MEDI QSM with LBV BFR was the most reproducible QSM reconstruction and Liu et al. who found that LBV was the most accurate BFR for non-linear MEDI, LBV was selected as the BFR method for all subsequent QSM reconstructions [35, 37]. Some additional changes were made to the QSM code including; better naming conventions for files and folders, adding the study ID obtained from DICOM tags to the produced QS map file names and backup files along with the method of BFR and masking to avoid potentially mixing these up, adding extra information to backup files to enable easy modification and testing of the various QSM parameters and settings and finally preparing the code for batch processing. High quality QS maps were then generated for all 121 subjects.

2.4 Coregistration & Automatic Segmentation of Caudate, GP, Putamen & Thalamus

The structural T_1-weighted images were segmented using FSL's FIRST automated segmentation. This procedure robustly and accurately identified the caudate, putamen, globus pallidus and thalamus and then generated 3D binary masks of these structures.

Because the structural T_1-weighted images and QSM images were acquired separately, there is a high potential for spatial mismatch between the two (e.g., because the subject moved) so the two images needed to be coregistered. This was performed using SPM12 by coregistering the magnitude image from QSM processing, which provides better contrast and more accurate anatomical detail than QSM for the purposes of coregistration, to the SPGR structural images. The changes to the header information that defined the position and orientation of the magnitude images can then be applied directly to the QSM images, which had the exact same spatial location and orientation as the uncoregistered magnitude images. The SPM12 coregistration accounts for both translation and rotation.

After coregistration the automatically segmented caudate, GP, putamen and thalamus masks (256x 256 x 170) were resliced with nearest neighbour interpolation using SPM12 to have the same resolution and number of slices as the QSM images (512 x 512 x 60). One can then apply those masks directly to QSM and extract the mean, median and standard deviation automatically for these structures. Because PD can be asymmetrical in its early stages the left and right structures were kept separate and were analysed individually [41].

2.5 SN & RN Masking

As was mentioned at the end of section 1.07, the SN and RN are almost invisible in structural T_1-weighted scans so one cannot automatically segment it using FSL FIRST. A different approach needs to be taken to segment these nuclei. The method used in this study followed a semi-automated process developed by Acosta-Cabronero et al. [42]. Firstly all the structural T_1-weighted scans were segmented again and DARTEL normalized using CAT12 and the deformation fields produced by the segmentation were used to normalise the structural images to Montreal

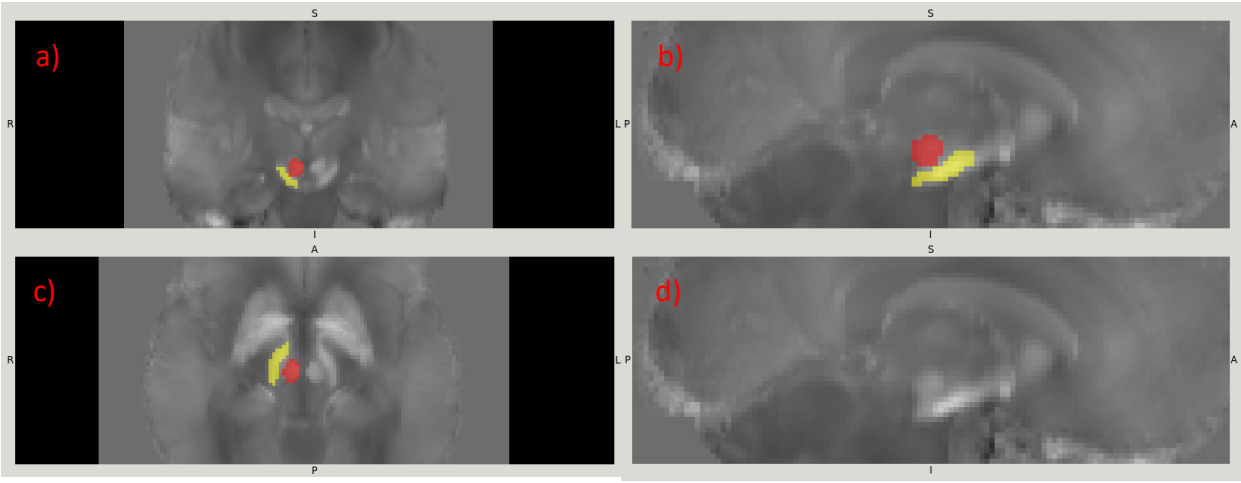

Figure 2.02a-d: SN masks (yellow) and RN masks (red) overlaid onto a HC QSM template normalised to MNI-152 space. a) Represents the coronal view, b) and d) the sagittal and c) the transverse view. The SN can be clearly made out on this QSM template. QSM images have a window and level of 0.5 and -0.25. Images were obtained from the New Zealand Brain Research institute (NZBRI).

Neurological Institute 152 (MNI-152) space using SPM12 and 5th degree B-spline interpolation. Normalisation involves warped registration of each patient's images to a template, In this case the MNI-152 template, which represents the average image, generated from a large data set. Normalisation removes the individual's shape and size dependency and allows one to directly compare values between subjects in each voxel. Since the QSM and structural images are coregistered the deformation fields generated from CAT12 segmentation can also be applied to the QSM images. A QSM control template was formed by obtaining the average voxel wise QSM value from the normalised QS maps of the 24 HCs. This template was then used to mask the SN and RN, which could be clearly seen (fig. 2.02a-d) using FSLView.

Although you can't see the SNc or SNr in individual T1 weighted scans it is actually possible to see the SN and distinguish the two segments in some T1 templates. The QSM control template SN masks were then overlaid onto another T_1 template, IXI555, which has some contrast between the SNc and SNr. In Fig 2.03c you can just make out a dark hypointense band on the outside that is the SNr (green arrow), and a lighter more hyperintense band between the hypointense region and the RN that is the SNc (blue arrow). By increasing the transparency of the masks in FSLView this and the RN that is the SNc. By increasing the transparency of the masks in FSLView this template was used to create a second mask of the SNr (fig. 2.03a-c). By subtracting the SNr mask from the whole SN mask one can obtain the SNc and hence separate the two portions of the SN (fig. 2.03a-c). By applying each subject's inverse normalisation deformation field to the SNc,

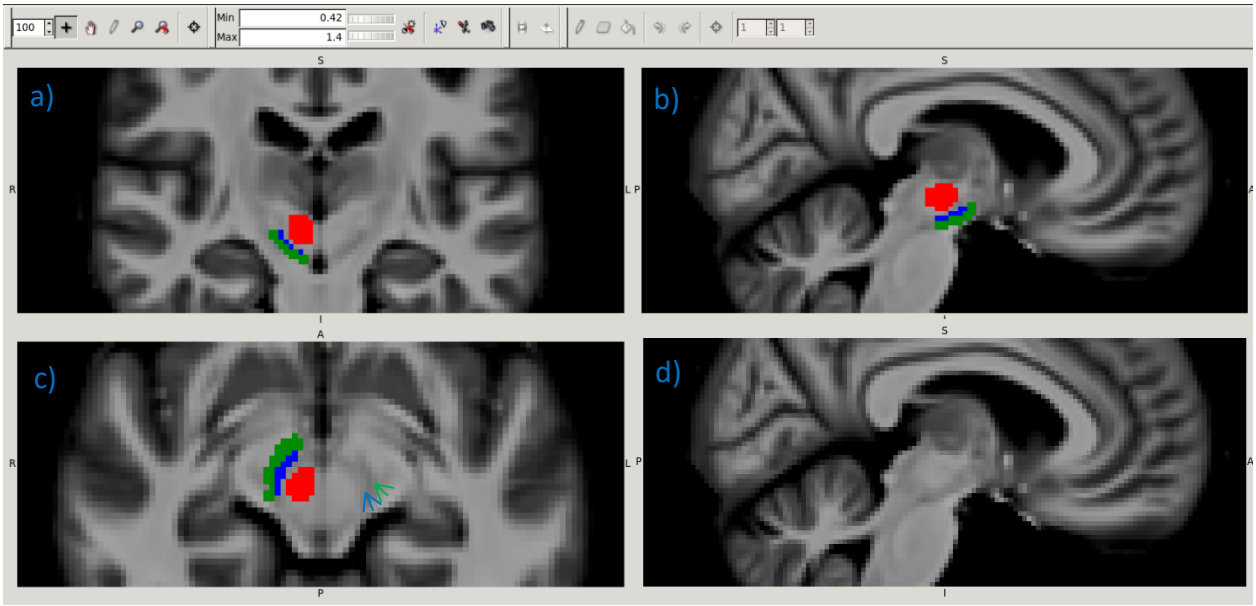

Figure 2.03a-d: Separation of the SN into SNr (green) and SNc (blue) using the IXI555 template. In Fig 2.03c you can make out a dark hypointense band on the outside that is the SNr indicated by a green arrow, a lighter more hyperintense band on the inside that is the SNc indicated by a blue arrow. By overlaying the masks produced in fig 2.02 onto the IXI555 template in FSLView and increasing their transparency we were able to identify the SNr, which was then subtracted from the whole SN mask in fig. 2.02 to obtain the SNc. Template images have a window and level of 0.4 and 1.4. Images were obtained from the New Zealand Brain Research institute (NZBRI).

SNr and RN masks we obtained individual masks for each of these structures in native subject space. This was performed using SPM12 with nearest neighbour interpolation. These masks were eroded by 1 voxel via convolution and were then applied to the original QSM images to extract values.

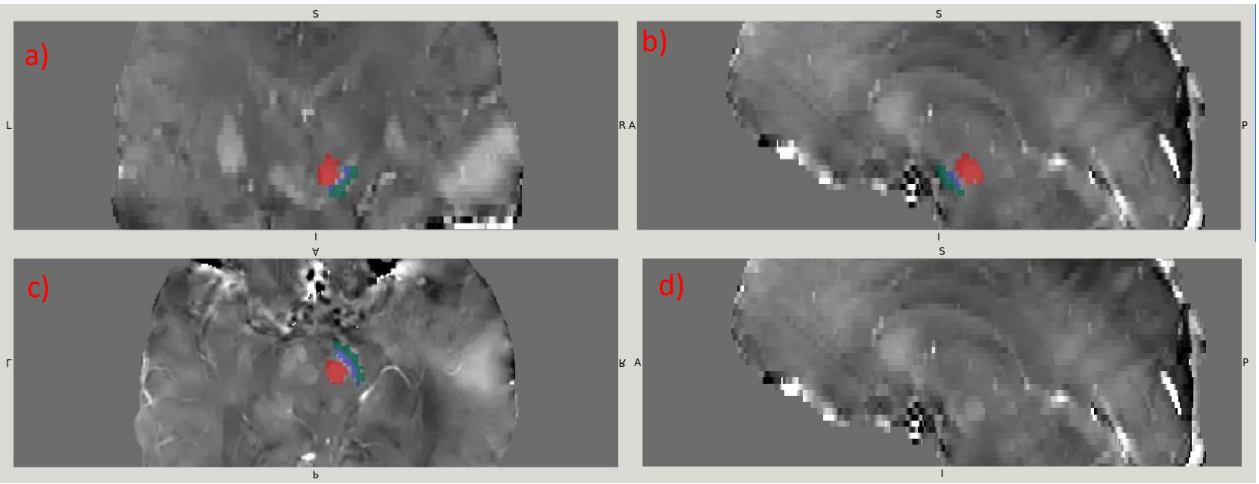

Figure 2.04a-c: An example of inverse warped RN (red), SNc (blue) and SNr (green) masks overlaid onto native QSM in the a) coronal view, b) sagittal view and c) axial view. d) is given as a reference for c) . As can be seen in figures 2.04a-c the masks do not exactly match the equivalent bright areas in native QSM. QSM images have a window and level of 0.5 and -0.25. Images were obtained from the New Zealand Brain Research institute (NZBRI).

As can be seen in fig. 2.04a-c the individual subject SN and RN masks were not perfectly aligned, however time restrictions meant this semi-automated method was the most viable option.

2.6 Bayesian Regression Modelling

QSM values were compared across group using Bayesian multi-level regression models with the *brms* (https://github.com/paul-buerkner/brms) package in R (v3.3.1). Varying intercepts were included per subject, modelling their QSM values in each scan and for each ROI. Subject-level predictors were group (control & PD) and sex; the session-level predictor was age; all predictors were estimated for each ROI. The priors for the predictors were Student-t distributions of degree 3, mean 0, standard deviation 1; similarly priors for the standard deviations were Student-t distributions of degree 4, mean 0, standard deviation 2. An additional model was fit including a session-level predictor of global CogZ to determine the association with cognition and QSM by region. This hierarchical Bayesian model reduces potential multiple comparisons issues by shrinking estimates [46]. This modelling technique has been successfully applied in humans in a longitudinal MRI study of cognitive decline in Parkinson's disease [47].

The first model was set up to test for the differences between PD as a whole group versus HCs for each region with sex and age as covariates.

Secondly we tested for any association between the four different categories, HCs, PD-N, PD-MCI and PDD, for each region with sex and age as covariates, accounting for any group differences discovered in the prior analysis. This will be the first time anyone has attempted this.

Additional analyses include testing for a correlation between QSM, global cognitive score (CogZ) UPDRS II, UPDRS III, and disease duration. The categories are derived from CogZ, but are also defined by the ability of the subject to perform daily tasks in living.

The QSM values given to the model were scaled up by a factor of 100 in order to delineate between borderline significant trends on the order of 0.01ppm. The estimates reported were divided by 100 and set to 3DP.

2.7 Whole Brain Analysis

With the normalised QSM images produced in section 2.5 it is possible to analyse QSM on a voxel by voxel basis and look for potential correlations between QSM and PD throughout the entire brain rather than on a structure by structure basis. This may give insight into the pathology underlying cognitive decline in PD. The following methodology was based on Acosta-Cabronero et al. [42].

The first step toward a whole brain analysis is obtaining a whole brain mask. This was achieved by simply obtaining each individual's white matter and gray matter masks produced by the CAT12 segmentation in section 2.5 and adding them together. These whole brain masks were then warped into MNI-152 normalised space using SPM12 and a 5^{th} degree B-spline interpolation. The normalised brain masks were binarized with a threshold of 0.5 and applied to the normalised QSM to remove cerebrospinal fluid and other non-neural tissues. Spatial smoothing is necessary prior to the whole brain analysis to smooth out residual coregistration errors and misalignments and to reduce the overall number of independent statistical tests. The normalised QSM and the normalised brain masks were then smoothed using SPM12 with a 3D Gaussian kernel of full width half maximum (FWHM) determined by the following equation [48],

$$\mathrm{FWHM} = \sigma\sqrt{8\ln(2)} \approx \sigma * 2.35$$

Where σ is the standard deviation in mm of the Gaussian kernel. Betts et al determined that a σ of 3mm was optimal for a QSM whole brain analysis giving a FWHM of 7mm [48]. The smoothed normalised QSM was then divided element wise by the smoothed mask to compensate for smoothing. The data was converted to a 4D NIfTI image file using SPM12 and was then ready to be analysed.

All voxel-wise comparisons implemented a general linear model, which are fundamentally different from the Bayesian ROI models. We tested whether PD showed increased QSM relative to controls using a t-test, implemented using 'randomise', a permutation based inference tool for non-parametric thresholding in FSL. For each contrast, the null distribution was generated over 10000 permutations at alpha level <0.05, correcting for multiple comparisons using threshold-free cluster enhancement [49]. Linear regression was employed to investigate the association between CogZ and voxel wise QSM with age, sex, and group (PD/Control) as covariates. The results of this linear regression were used to identify whether any significant correlations with cognition exist for QSM.

The first linear regression model was made up of two contrasts testing the null hypothesis that QSM values are not different between PD and HCs with age and sex as covariates. The fist contrast was PD > HC

$$Y = \beta_{PD} - \beta_{HC} + 0\beta_{sex} + 0\,\beta_{age}$$

And the second, PD < HC,

$$Y = \beta_{HC} - \beta_{PD} + 0\beta_{sex} + 0\,\beta_{age}$$

The second linear regression model was made up of two contrasts testing the null hypothesis that there is no association between cognition and QSM with age, sex, and group as covariates. The first contrast tested whether a positive association exists:

$$Y = \beta_{cog} + 0\beta_{sex} + 0\,\beta_{age} + 0\,\beta_{group}$$

And the second whether a negative association exists,

$$Y = -\beta_{cog} + 0\beta_{sex} + 0\,\beta_{age} + 0\,\beta_{group}$$

Chapter 3: Results

Results from the Bayesian regression models will be reported first. Reported results will include the estimate of the effect, and its associated error. If the 95% confidence interval of the estimate does not cross zero, than the estimate is considered statistically significant in the classical sense (at $p<0.05$).

3.1 Age and Sex Dependence

First, age and sex effects are reported from the following model (table 3.01 and figure 3.01):

```
qsm_model <- brm(QSM_dm_su100 ~ Region:age_s100 + Region:sex + Region + group:Region +
(1|nzbri_id),
        control = list(adapt_delta = 0.99),
          prior = c(set_prior("student_t(4,0,2)", class = "sd"),
                set_prior("student_t(4,0,2)", class = "sigma"),
                set_prior("student_t(3,0,1)", class = "b")),
        data=w, algorithm = c("sampling"))
summary(qsm_model, waic = TRUE),
```

Where Region:age_s100 models the region by age interaction; Region:sex, the region by sex interaction; and group:Region, the group by region interaction.

QSM and sex:

Region	Estimate (ppm)	Estimate Error (ppm)	Lower 95% (ppm)	Upper 95% (ppm)
Intercept	0.005	0.005	-0.005	0.015
Left caudate	-0.012	0.005	-0.023	-0.002
Left GP	-0.005	0.006	-0.017	0.006
Left putamen	-0.007	0.006	-0.018	0.004
Left RN	-0.008	0.006	-0.020	0.003
Left SNc	0.004	0.005	-0.007	0.014
Left SNr	0.000	0.005	-0.011	0.011
Left thalamus	0.005	0.006	-0.006	0.016
Right caudate	-0.003	0.005	-0.013	0.007
Right GP	-0.001	0.005	-0.011	0.010
Right putamen	-0.001	0.005	-0.012	0.009
Right RN	-0.012	0.006	-0.025	-0.001
Right SNc	-0.003	0.005	-0.014	0.007
Right SNr	-0.001	0.005	-0.012	0.010
Right thalamus	0.000	0.006	-0.011	0.009

Table 3.01: Summary of results from the group model for sex and mean QSM. All values are expressed in ppm (parts per million) with female as the reference for the model. The left caudate and right RN had 95% confidence intervals that did not cross 0, implying statistically significant reductions in QSM in males compared to females in these nuclei.

There was a small, but borderline significant reduction in mean QSM of the left caudate, and right RN in males compared to females (table 3.01 & figure 3.01), but this is of little clinical importance.

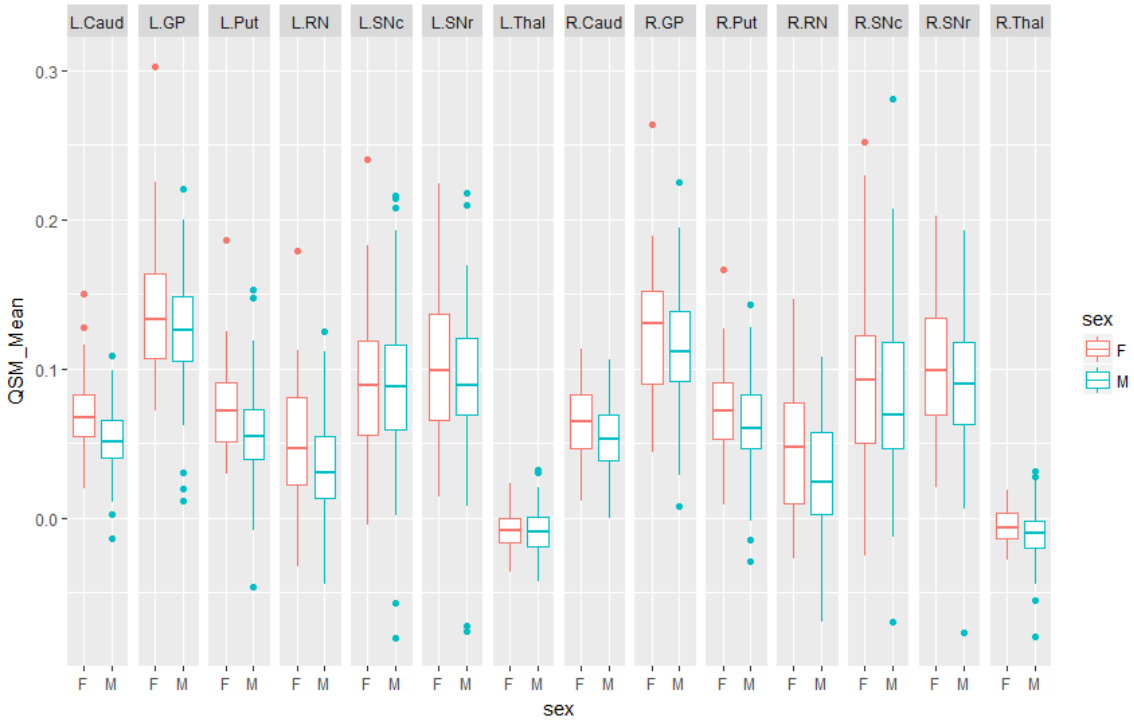

Figure 3.01: Boxplots of mean QSM in each region for males (M) and females (F). Males appear to have lower QSM than females in the left caudate, and right RN.

QSM and Age:

Region	Estimate (ppm)	Estimate Error (ppm)	Lower 95% (ppm)	Upper 95% (ppm)
Intercept	0.005	0.005	-0.005	0.015
Left caudate	0.004	0.014	-0.021	0.035
Left GP	0.007	0.016	-0.018	0.047
Left putamen	0.050	0.049	-0.006	0.162
Left RN	-0.010	0.018	-0.059	0.014
Left SNc	-0.001	0.013	-0.030	0.027
Left SNr	-0.001	0.013	-0.029	0.025
Left thalamus	0.000	0.013	-0.026	0.025
Right caudate	-0.004	0.014	-0.037	0.021
Right GP	0.001	0.012	-0.024	0.027
Right putamen	0.018	0.027	-0.013	0.091
Right RN	-0.054	0.051	-0.169	0.006
Right SNc	-0.003	0.014	-0.034	0.023
Right SNr	-0.002	0.013	-0.030	0.024
Right thalamus	0.000	0.013	-0.027	0.026

Table 3.02: The relationship between mean QSM and age in each region. The left and right putamen produced large increases in QSM with increasing age, but these were found to be not significant.

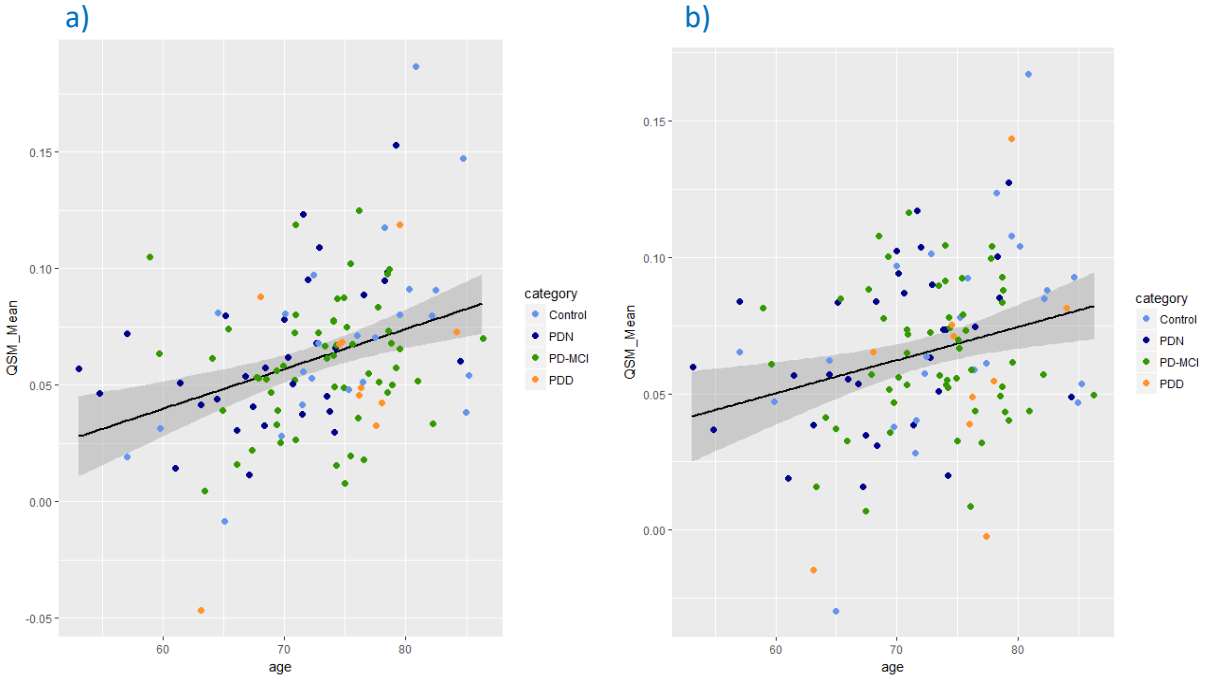

Figure 3.02a & b: Plots of mean QSM with age in the left (a) and right (b) putamen, with a linear regression fit demonstrating a linear increase in QSM with age in these two structures. The grey area indicates 2 standard deviations. The various categories are included with colour coding to provide extra information however there seems to be no pattern or grouping within the categories.

Despite seeing a notable age related increase in QSM in the left and right putamen (fig. 3.02a&b), this was found to be not significant in the model's analysis (table 3.02).

3.2 Group Analysis

The first major comparison was the group comparison, PD as a whole vs. HCs, from the model in 3.1. We saw a significant increase in QSM in the left and right SNc (fig. 3.03, 3.04 & table 3.03). While QSM was significantly increased in PD, notice the substantial overlap in fig. 3.03 a & b and fig. 3.04. No other structures showed any significant differences between PD and HCs.

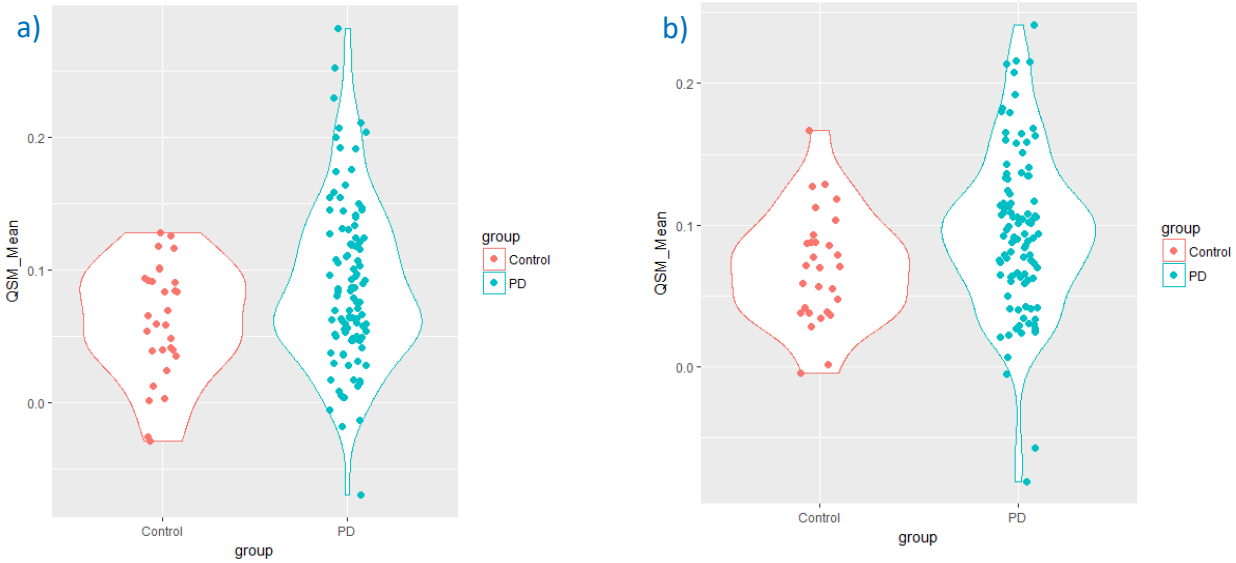

Figure 3.03a & b: Violin plots of the left (a) and right (b) SNc demonstrating the increased mean QSM for PD compared to controls.

Region	Estimate (ppm)	Estimate Error (ppm)	Lower 95% (ppm)	Upper 95% (ppm)
Intercept	0.005	0.005	-0.005	0.015
Left caudate	-0.004	0.005	-0.015	0.006
Left GP	0.001	0.006	-0.011	0.013
Left putamen	-0.007	0.006	-0.019	0.004
Left RN	-0.001	0.006	-0.012	0.011
Left SNc	0.020	0.007	0.007	0.034
Left SNr	0.009	0.006	-0.002	0.022
Left thalamus	-0.006	0.006	-0.018	0.006
Right caudate	-0.008	0.006	-0.021	0.003
Right GP	0.003	0.006	-0.008	0.015
Right putamen	-0.006	0.006	-0.018	0.004
Right RN	-0.003	0.006	-0.015	0.009
Right SNc	0.018	0.007	0.005	0.031
Right SNr	0.004	0.006	-0.007	0.016
Right thalamus	-0.003	0.006	-0.015	0.009

Table 3.03: Summary of results from the group analysis. A statistically significant increase in mean QSM was observed in the left and right SNc for PD compared to HCs. No other nuclei demonstrated significant differences.

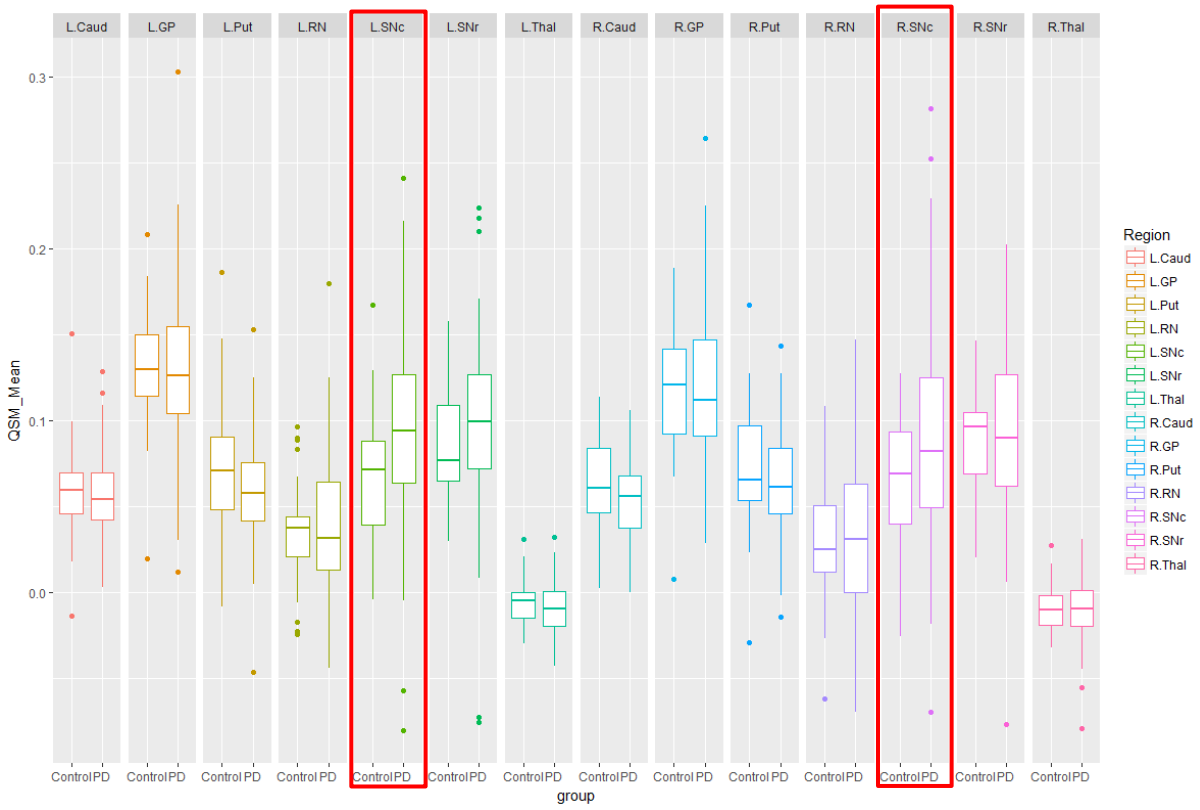

Figure 3.04: Boxplots of mean QSM for PD and controls in each region. PD showed a statistically significant increased mean QSM in the SNc compared to controls. The other structures show no statistical significance in their differences.

3.3 Category Analysis

Next the different cognitive categories were modelled using the following,

```
w_nan <- subset(w,!is.na(w$category))
w_nan <- subset(w,w$category!="Control-MCI")
qsm_model_cog <- brm(QSM_dm_su100 ~ Region:age_s100 + Region:sex + Region +
category:Region + (1|nzbri_id),
        control = list(adapt_delta = 0.99),
        prior = c(set_prior("student_t(4,0,2)", class = "sd"),
                set_prior("student_t(4,0,2)", class = "sigma"),
                set_prior("student_t(3,0,1)", class = "b")),
        data=w_nan, algorithm = c("sampling"))
summary(qsm_model_cog, waic = TRUE),
```

Where category:Region models the interactions between cognitive categories in PD and HCs.

Fig. 3.05 displays the raw data by category. There doesn't seem to be any significant trends between categories outside of PD as a whole and controls in the SNc. From the model we see an increase in left SNc mean QSM in PD-N compared to HCs, but not in the right SNc and the significant left SNc elevated QSM disappears with PD-MCI and PDD (Table 3.04). Note for the right SNc in PD-N the lower bound for the confidence interval is -0. This is because when the results were scaled up this value was found to be slightly less than zero, however when scaled back to the original units this small negative value was rounded to zero. The negative indicates that this confidence interval has in fact crossed zero. Due to the large volume of data in the category analysis just the left and right SNc is displayed in table 3.04. All the data is available in table A1, in Appendix A.

	Region	**Estimate (ppm)**	**Estimate Error (ppm)**	**lower 95% (ppm)**	**upper 95% (ppm)**
	Intercept	0.006	0.005	-0.005	0.016
PDN	Left SNc	0.02	0.008	0.005	0.037
	Right SNc	0.013	0.007	-0	0.028
PD-MCI	Left SNc	0.011	0.007	-0.001	0.025
	Right SNc	0.01	0.006	-0.001	0.023
PDD	Left SNc	0.001	0.008	-0.014	0.018
	Right SNc	-0.001	0.008	-0.017	0.015

Table 3.04: Summary of results from the group analysis. A statistically significant increase in mean QSM was only observed in the left SNc for PD-N compared to HCs. Note for the right SNc in PD-N the lower bound for the confidence interval is -0. This is because when the results were scaled up this value was found to be slightly less than zero, however when scaled back to the original units this value was rounded to zero. The negative indicates that this confidence interval has in fact crossed zero. For the sake of simplicity just the SNc is displayed in table 3.04. All the data from the category model is available in table A1, in Appendix A.

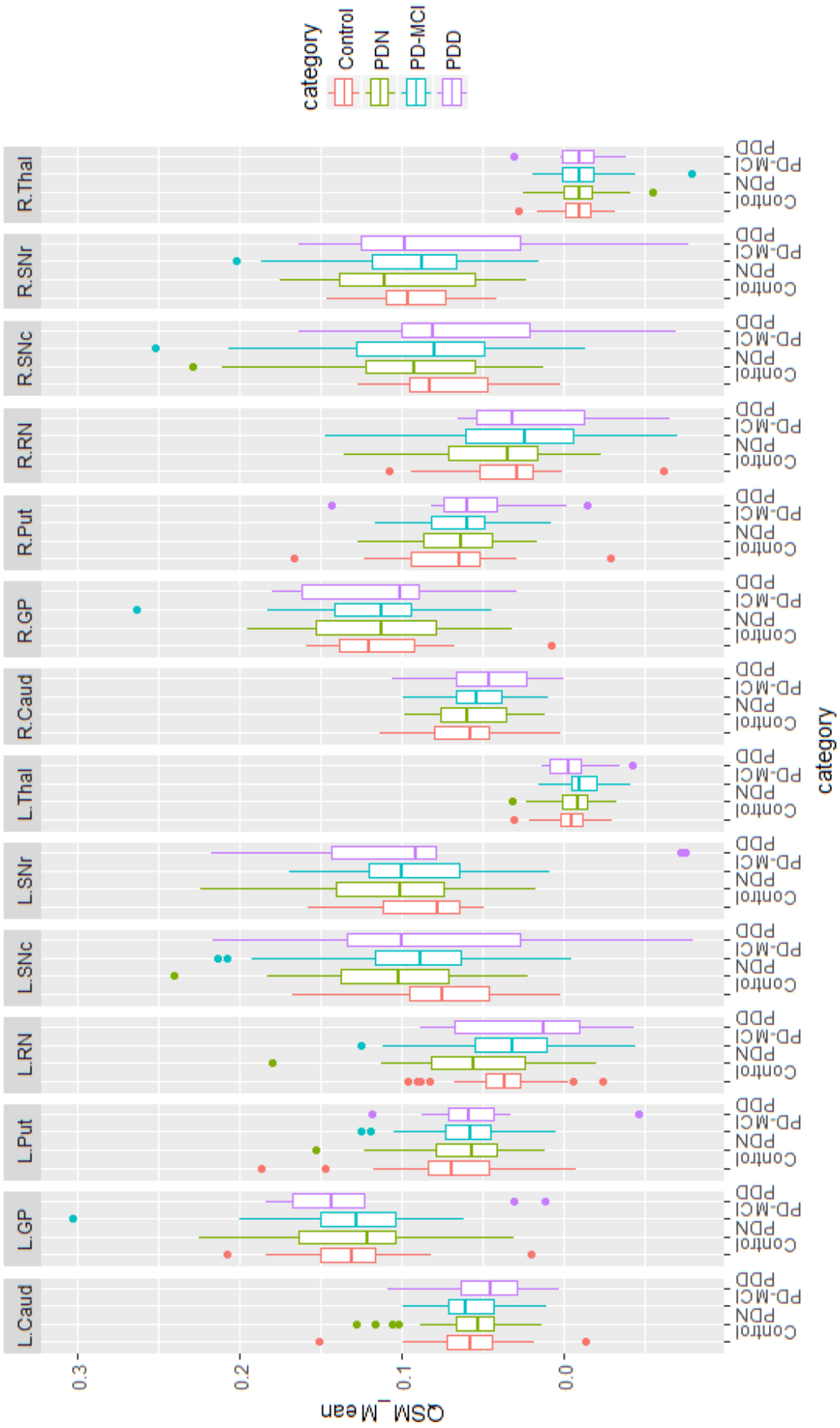

Figure 3.05: Box plots of mean QSM for each category in each structure investigated. To the naked eye there doesn't appear to be any significant trends between categories.

3.4 Additional Analyses

The relationship between cognition and QSM was further investigated via the following model:

```
qsm_model_cog <- brm(QSM_dm_su100 ~ Region:age_s100 + Region:sex + Region + Region:Group + cogz:Region + (1|nzbri_id),
        control = list(adapt_delta = 0.99),
        prior = c(set_prior("student_t(4,0,2)", class = "sd"),
                set_prior("student_t(4,0,2)", class = "sigma"),
                set_prior("student_t(3,0,1)", class = "b")),
        data=w, algorithm = c("sampling"))
summary(qsm_model_cog, waic = TRUE)
```

This differs from the previous group model in 3.2 by the inclusion of a CogZ by region interaction, allowing the investigation of the association between QSM and global cognitive score in each region. This models cognition as a continuous variable as opposed to categories.

Increased QSM in the SNc was found to persist with PD confirming the result from 3.2 (table A2, Appendix A). Additionally the left SNr also showed a significant increase, but this was borderline (table 3.05). There is a slight increase in CogZ with increasing mean QSM in the right RN, but the evidence is weak (table 3.05).

Region	Estimate (ppm)	Estimate Error (ppm)	Lower 95% (ppm)	Upper 95% (ppm)
Intercept	0.006	0.005	-0.004	0.016
Left caudate	-0.003	0.003	-0.009	0.004
Left GP	-0.003	0.003	-0.009	0.004
Left putamen	-0.004	0.004	-0.011	0.003
Left RN	0.005	0.003	-0.002	0.012
Left SNc	0.002	0.004	-0.006	0.008
Left SNr	0.003	0.004	-0.004	0.010
Left thalamus	0.000	0.004	-0.007	0.007
Right caudate	0.002	0.003	-0.005	0.008
Right GP	-0.001	0.003	-0.008	0.006
Right putamen	-0.002	0.004	-0.009	0.004
Right RN	0.008	0.004	0.001	0.016
Right SNc	0.005	0.004	-0.002	0.012
Right SNr	0.006	0.004	-0.002	0.013
Right thalamus	0.000	0.004	-0.007	0.007

Table 3.05: Summary of the trends between CogZ and mean QSM in each nuclei. A small, but significant increase in CogZ with increasing QSM was noted in the right RN.

The UPDRS-II and UPDRS-III models both came back with no correlations of statistical significance (Table A3 & 4, Appendix A). Disease duration also showed no trends of significance (fig 3.06b and table A5, Appendix A).

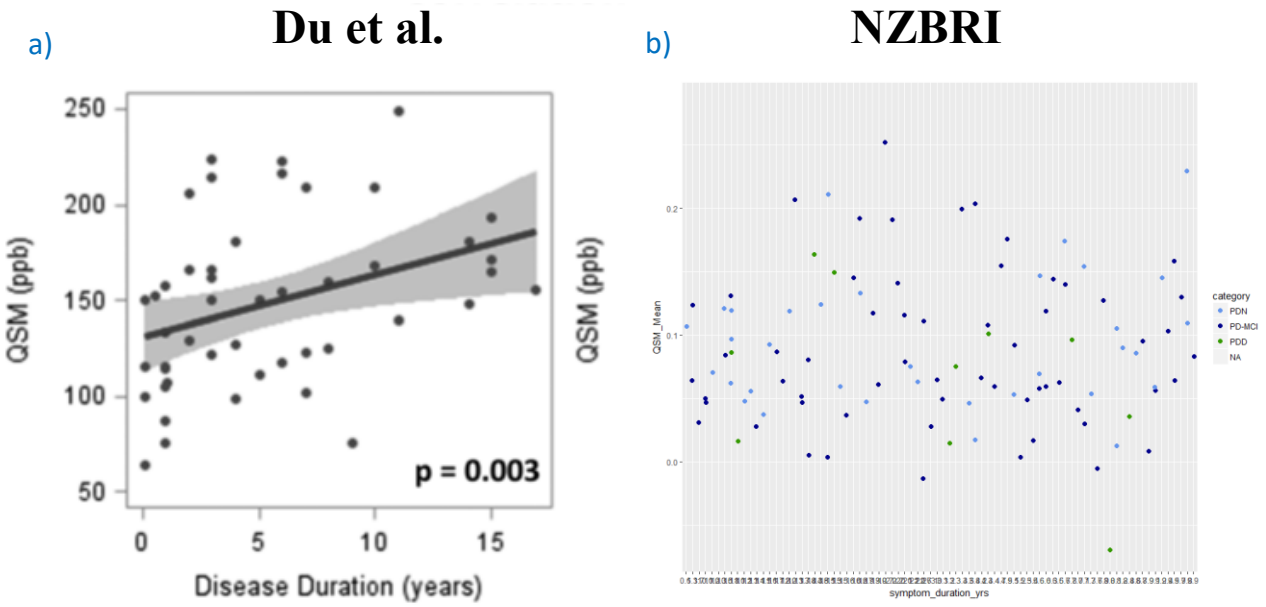

Figure 3.06a & b: a) Left SNc QSM (ppb) plotted against disease duration undertaken by Du et al [39]. b) LSNc QSM (ppm) plotted against disease duration in years undertaken at the NZBRI. Unlike Du et al. our data appears to be no more than random scatter.

3.5 Whole Brain Analysis

The whole brain analyses did not reveal any regions of statistical significance ($p>0.095$). That is, no differences between groups or association with cognitive score survived correction for multiple comparisons.

Chapter 4: Discussion

4.1 Age and Sex Dependence

There were some unexpected sex dependences on mean QSM discovered in the first analysis (table 3.01 & figure 3.01), which as far as I know have not been reported or discussed. Although the estimates are small and borderline due to confidence interval's proximity to zero, there may be some underlying physiological basis to this trend.

There was a noticeable increase in mean QSM of the left and right putamen with age (fig. 3.02a & b), however this was found to be not significant. The BG can contain microbleeds which are hyperintense (paramagnetic) and calcifications which are hypointense (diamagnetic) and appear in QSM as white and black dots, respectively. Both are capable of creating significant outliers

that can affect the mean. Microbleeds in the putamen such as the one in fig. 4.1b are more common with age and may explain this age related trend in mean QSM in the putamen for the linear plots of fig. 3.02 a & b.

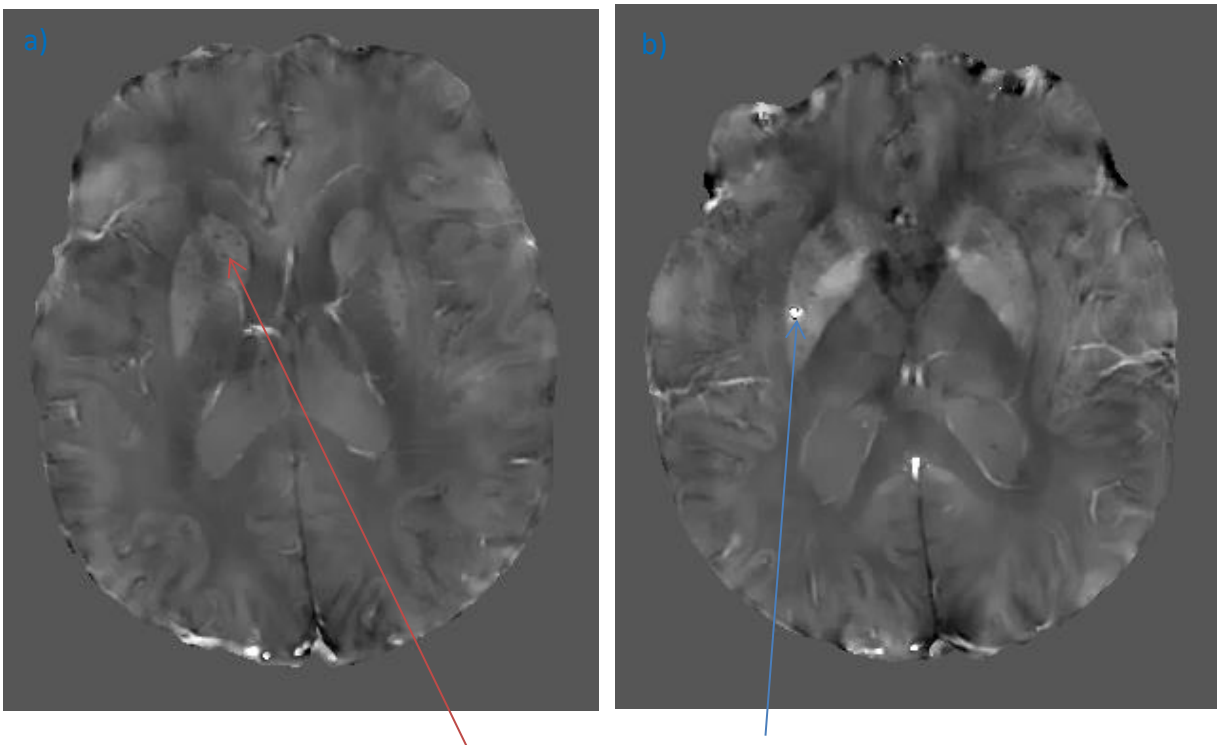

Figure 4.1a & b: An example of microcalcification (a) and a microbleed (b), which are both related to cerebrovascular disease. Microcalcifications are small calcium deposits, which are quite strongly diamagnetic and appear black in QSM. Microbleeds are small localised strokes and the blood that pools there is strongly paramagnetic. The QSM images have a window and level of 0.5 and -0.25. Images were obtained from the New Zealand Brain Research institute (NZBRI).

4.2 Group Analysis

We saw an increase in the SNc mean QSM of PD compared to HC, which agrees with all previous studies of QSM and PD [38, 39, 40, 41, 42]. This result effectively verifies that QSM has been correctly reconstructed and adequately analysed. As you can see in Fig 3.03a & b PD and HCs aren't separated by very much in the SNc. Our estimates of the difference between mean QSM in left and right SNc for PD and HCs (~0.022 [0.008, 0.038]ppm) was lower than that of Du et al. (0.04±0.04ppm) [39]. Du also used a PD population that was in less advanced stages of the disease on average, which in theory would have led to a lower QSM group difference than what we obtained, however Du did not correct for multiple comparisons [39]. Misalignment of SN masking in the current study may have also contributed to this difference. Variable SN masking may be due, in part, to the HC template not representing the entire population as a whole, residual coregistration and normalisation error that is significant when investigating a structure as small as the SN and the IXI555 template (healthy population with a mean age of ~23years) not fully

representing the population being studied (PD with a mean age 72 years). The controls were specifically used for the QSM template due to PD affecting the shape and size of the SN, which could then not be related to a healthy template like IXI555. Therefore the HCs offered the best estimate of an anatomical definition of the SN on the IXI555 template. Given that increasing QSM in the SN had already been correlated to PD progression and that partial voluming effects increases the size of high QSM structures it was believed that the SN and RN masks would inherently be within the confines of their respective structures for PD QSM [23, 40]. However the resultant lack of accuracy in SN and RN masking in PD has probably occurred for the same reasons PD subjects were not used for the QSM template; there is most likely changes to the anatomy in PD due to neural atrophy [6].

All the ROI studies performed thus far for QSM and PD had the nuclei investigated masked manually by an experienced radiologist either in the most representative slice [38, 40] or for the entire volume [39, 41] on QSM directly or using the template method and altering the masks after inverse normalisation [42] and as a result may be more accurate. While inverse normalization of SN and RN masks in normalized space have been used effectively in recent publications, hence our choice in using this method, manually-delineated SN and RN may have been more precise.

It should also be noted whenever comparing past studies to this work that no other QSM study has used our method of statistical analysis, which may explain any discrepancy between the observed results in this study and others. The Bayesian regression model and correction for multiple comparisons is a much more accurate way of evaluating potential correlations [47].

4.3 Category Analysis

The category analysis yielded just a single significant increase in the left SNc for PD-N. The presence of a significant increase in mean QSM for PD-N, but a lack of this increase in SNc for PD-MCI and PDD indicates that there may be a secondary process occurring which may affect patients as dementia develops. However misalignment of SN & RN masks, as outlined in section 4.2, has likely contributed to this difference including surrounding non-SN and RN tissues, which have likely reduced the mean QSM in these nuclei. From a masking point of view there is little ambiguity for the results of the caudate, GP, putamen and thalamus in our category analysis and hence the evidence we have gathered suggests that there is no correlation between QSM and cognition in these nuclei.

Guan et al. noted an increase in the SNr and GP mean QSM (specifically the internal GP) in addition to the SNc in late PD (Hoehn & Yahr>3) [40]. All of the PDD subjects in our population

had Hoehn and Yahr scores greater than 3, but we did not see these associations for PDD. SN masking misalignment likely accounts for the SNr and unfortunately, despite using much more accurate automatic segmentation for the GP, we did not differentiate between the internal and external GP. Other than not separating the GP one difference in methodology that could account for this discrepancy is the lack of correction for multiple comparisons in Guan's study [40], however there are more sources of error in QSM itself, which should be taken into consideration:

1. Field inhomogeneities or motion is capable of inducing arteficial phase shifts and signal. Because we are dealing with patients that have developed PD there will be some level of involuntary movement that we can't realistically avoid. The involuntary movement can be partially treated, however the patients are in the scanner for almost an hour during which it is difficult to continue any medication and the time of QSM scanning within a session can vary.
2. There is Gaussian noise in the receiver MRI coils.
3. The thickness of our slices is quite significant leading to masking inaccuracies and averaging with tissues outside of the ROIs in the vicinity of nuclei boundaries.
4. Levodopa dosage has shown a correlation with QSM but wasn't corrected for in this study.
5. The ill-posed nature of QSM reconstruction introduces a relatively high level of uncertainty.

As a result the standard deviation of QSM was consistently around the 30% mark, which is normal for QSM [39]. With a level of uncertainty this high significant variation can be expected between studies even with large sample sizes.

Previous correlations in structures outside the SNc may have been due to using a single representative slice instead of averaging over the entire anatomical volume [40]. Although single slice extraction can be seen as 'cherry picking' to some degree without physiological basis, it may be possible that iron deposition is localised within a nuclei and that averaging across the entire anatomical volume is simply averaging the deposition with other regions without any deposition and hence missing any potential markers of disease in that structure. There appears to be quite a lot of difference between the anatomical outlines of nuclei from T1 and those in QSM where nuclei are clearly visible (fig. 1.16c & d). Perhaps even though QSM is affected by partial voluming effects it may offer some extra insight into the deeper pathology of the disease. Perhaps QSM should be trusted more for identifying the true sites of PD pathology within its own images.

The disappearance of the right SNc significant increase in QSM for PD-N may be due to asymmetry. PD in its early stages is asymmetrical with one side affected more than the other [6]. The problem with grouping structures as left and right is the affected side varies. It's possible that half the left structures of the brain are on the affected side and the other half are not blurring any potential differences between nuclei. Despite the asymmetrical onset of early PD Barbosa and He et al found no asymmetry in QSM between the affected and non-affected sides in early PD (Hoehn and Yahr<1) [38, 41]. Side affected data was available, but unfortunately it is unreliable due to its dependence on patient reports in many cases and is not available for every subject. The side affected analysis has another complication in that people are naturally left or right hand dominant and show asymmetry because of hand dominance without disease. When looking at which side is affected you also need to account for whether they are left or right handed, which wasn't noted when our clinical trials were performed.

4.4 Additional Analyses

The CogZ model gave the same group based increase in the SNc as section 3.2 reaffirming this result. The CogZ model also returned a weak positive trend with mean QSM in the right RN. The RN has no known physiological role in cognition. Even so iron deposition and hence neurodegeneration with PD should lead to a reduction in cognition and therefore in CogZ resulting in a negative association not a positive association. This result for CogZ is also likely to be influenced by misalignment of masking of the SN and RN already mentioned in section 4.2 and 4.3.

Unlike Du and He et al we did not see any correlations with UPDRS II or III [39, 41]. A major factor in the discrepancy between our results and their findings is that we used a correction for multiple comparisons. It should also be noted that UPDRS-II and III clinical trials do also have some associated uncertainty. For UPDRS-II the results are somewhat subjective to the patient and for UPDRS-III the performance of the subject can vary from day to day due to random variation and mood [14]. Different clinicians can also score the patients on UPDRS-III differently for reasons cited in section 1.04.

Several studies have found a correlation between disease duration and QSM in the SNc, which we did not observe (fig.3.06a & b) [39, 41]. A study by Jin et al. contradicted this finding noting no significant correlation between QSM and disease duration [50]. This discrepancy was put down to differences in SN masking and hence our result is also likely affected by masking inaccuracies as outlined in section 4.2.

4.5 Whole Brain Analysis

Acosta-Cabronero observed significant differences in QSM between PD and HCs in multiple regions of the brain including parts of temporal, paralimbic, occipto-parietal & prefrontal cortices as well as the rostral pontine area [42]. Our results didn't show any significance anywhere in the brain both for the PD and control group analysis and the CogZ analysis. Acosta-Cabronero also did not correct for multiple comparisons, but it is likely our results were affected by artefacts. There were a number of background field artefacts present around the border of the QSM images and where sinuses had been included in the brain mask by mistake that could not be avoided without manual intervention. The whole brain analysis is also very sensitive to co-registration errors, which could be improved [42]. The reproducibility of the whole brain is unexplored and likely worse than any of the 7 nuclei we have investigated due to the inclusion of tissues in close proximity to the skull and air interfaces and hence the source of the background field. Extreme values on the fringe of the QS maps were quite frequently observed where brain masking had not quite excluded all tissues outside of the brain such as cerebrospinal fluid.

4.6 Future developments

As mentioned in section 4.1 cerebrovascular disease is capable of drastically altering QSM especially in the striatum and GP. This might explain why in fig. 3.05 the PDD category, where cerebrovascular disease is much more common, had a slightly lower QSM in the right and left caudate than the other categories. Ideally if these patients do have cerebrovascular disease they would be excluded, but there is a natural level of calcification and microbleeding with age and proper diagnosis is not at our disposal. Also cerebrovascular disease is most common in PDD, of which we only had 10 subjects (table 2.1). It is however possible to work around the disease. Both microbleeds and calcifications are highly localised and have distinct outlying values. It may be possible to exclude these pathologies from the means and medians of ROIs by finding the average minimum and maximum QSM in PD patients of varying PD severity and duration, but without cerebrovascular disease, and the standard deviation of these minimums and maximums, for each of the ROIs being investigated. Using the obtained minimum and maximum values one could form windows of the minimum -2 standard deviations to the maximum +2 standard deviations, and any values that are outside of this window such as cerebrovascular disease outliers could be excluded from the mean or median for that ROI. This would allow subjects with cerebrovascular disease that are predominantly PDD and who already have very limited availability to still be included in PD QSM research.

To clarify the effect of side affected on the category analysis, especially for early PD, a sideaffected analysis accounting for left and right hand dominance should be undertaken with correction for multiple comparisons. Also analysing the internal and external GP individually in the category model may reveal a positive correlation with QSM such as that discovered by Guan et al., which may be related to cognition [40].

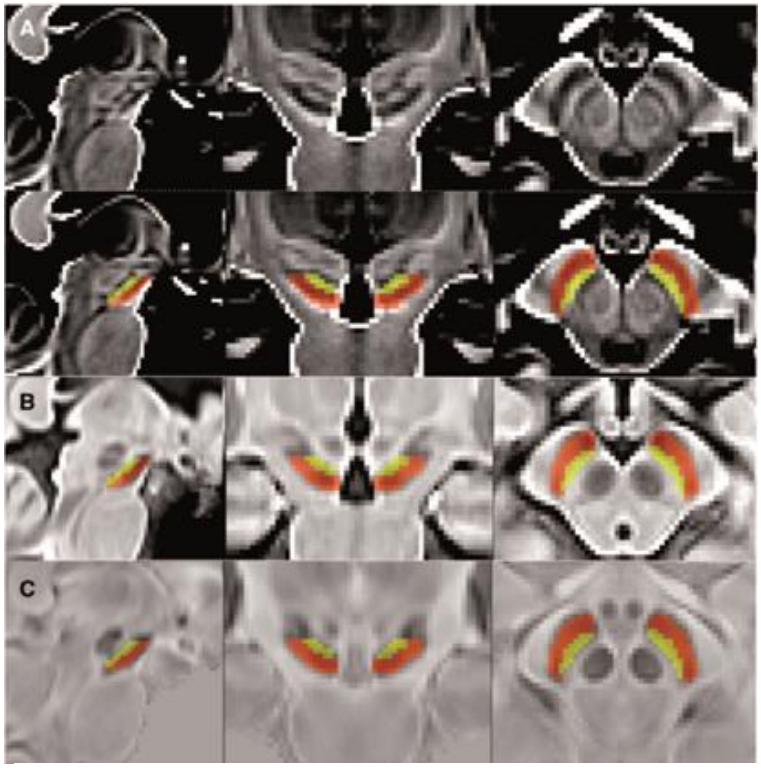

Figure 4.2: Acosta-Cabronero's T_1 template and overlaid SNc (yellow) and SNr (red) masks. A is the T_1 template, B is a magnitude image template, and C is the QSM template. Note that the contrast and appearance of the SNr and SNc in A is greatly different from that of fig. 2.03c. [42].

We were unable to reproduce the contrast present in the T_1 template Acosta-Cabronero used when he separated the SN. Using the IXI555 template I could make out a rough darker area on the outside of the transverse view (fig2.03c), a lighter band in between before the RN, but it was nothing like Acosta-Cabronero's template (fig 4.2) and it was of lower resolution. Using Acosta-Cabronero's template could provide a better idea of the spatial position of the SNc and SNr and improve these masks. Alternatively the inverse warped SN and RN masks could be manually altered to ensure they match up with the equivalent structure on the individual subject's normalized QSM providing more accurate estimates of mean QSM in the SN and RN [42]. It would be useful to repeat our analyses with single slice manually drawn masks for each structure to see if we get the same results as the other single slice studies. Also better brain masks may be able to reduce artefacts present in the whole brain analysis along with improved coregistration.

Iron concentration and therefore mean QSM has been correlated to PD duration and is seen to be significantly higher in the SNc of early PD patients then in HC [41]. These findings along with the fact that 50-80% of SNc cell loss occurs before any PD symptoms even arise means that it is likely that iron accumulation and elevated iron concentration in the SNc can be detected before PD even develops or shows symptoms [6]. If the relationship between iron deposition and SNc cell loss is linear prior to disease development and is significantly higher than that of healthy individuals this would give rise to the possibility of forming a PD prognosis with QSM, which

would allow the trial and application of an intervention to prevent PD progression. There are several interventions already being proposed including iron chelators, which became the first therapy found to delay PD progression [51].

Santin et al tested various QSM techniques to check the reproducibility of QSM and found the within and between subject variation due to set up differences, and individual variability to be sufficiently small as to enable longitudinal studies with realistic populations [37]. However with only 1% of the population over 60 developing PD, to prove that PD can be predicted by SNc QSM you would need a longitudinal study of the order of several thousand healthy individuals to achieve a large enough PD sample size to be able to prove there is a correlation and analyse its significance [4, 37]. Also the subjects used in Santin's study were healthy and hence did not take into account reduced reproducibility due to motion of PD patients during scanning [37]. With involuntary tremors motion is practically inevitable and unavoidable even if treated with medication so this would need to be investigated to be sure that QSM in PD is adequately reproducible for longitudinal PD tracking.

Chapter 5: Conclusion

In conclusion we have found significant increases in the left and right SNc in PD when compared to healthy age and sex matched controls, which agrees with the literature. From the evidence we have gathered there doesn't seem to be any association between QSM and cognition. We did not observe a disease duration correlation for SNc, which disagrees with the literature and the weak correlation found between CogZ and QSM was the opposite of what we expected in terms of the known physiology, however differences in the statistical analyses used in this study and others may account for the discrepancies observed. It is likely that any correlations in the SN and RN are influenced by poor masking. In the future we hope to improve the SN & RN masking and further investigate the impact of single slice masking and separation of the GP into its internal and external segments on the relationship between QSM, cognition and PD.

Chapter 6: Bibliography

1. Parkinson J. *An Essay on the Shaking Palsy*. London: Whittingham and Rowland for Sherwood, Neely, and Jones; 1817.

2. de Lau LML, Breteler MMB. *Epidemiology of Parkinson's disease*. Lancet Neurol. 2006; 5:525–35.

3. Parkinson's New Zealand, http://www.parkinsons.org.nz/, accessed on 31/05/16

4. Population ageing in New Zealand, http://www.stats.govt.nz/browse_for_stats/people_and_communities/older_people/pop-ageing-in-nz.aspx., accessed on 31/05/16

5. Health Loss in New Zealand 1990-2013, http://www.health.govt.nz/system/files/documents/publications/health-loss-in-new-zealand-1990-2013-aug16.pdf, accessed on 31/05/16 , accessed 31/05/16.

6. D. Purves, G J. Augustine, D Fitzpatrick, W.C. Hall, A. LaMantia, J. O. McNamara, M. Williams, *Neuroscience 3rd Ed.*, Ch. 6 pg. 148-150 to 257 & 262 & 283 to 309. Sinauer Associates, Inc. 2004.

7. Mark R. Cookson, *Parkinsonism Due to Mutations in PINK1, Parkin, and DJ-1 and Oxidative Stress and Mitochondrial Pathways*, Cold Spring Harb Perspect Med. 2012 Sep; 2(9).

8. Marella M., Seo BB, Yagi T, Matsuno-Yagi A., *Parkinson's disease and mitochondrial complex I: a perspective on the Ndi1 therapy.* J Bioenerg Biomembr. 2009 Dec;41(6):493-7.

9. Braak H, Ghebremedhin E, Rub U, Bratzke H, Del Tredici K. *Stages in the development of Parkinson's disease-related pathology*. Cell Tissue Res 2004; 318: 121–34.

10. Dexter D., Wells F. R., Agid F., et al. *Increased nigral iron content in post-mortem Parkinsonian brain*. Lancet 1987;2(8569):1219–20.

11. M. F. Bear, B. W. Connors, M. A. Paradiso, *Neuroscience, Exploring the Brain, 3rd Ed.* Lippincott Williams & Wilkins, 2007.

12. Sian-Huelsmann J, Mandel S, Youdim MB, Riederer P. *The relevance of iron in the pathogenesis of Parkinson's disease*. J Neurochem 2011; 118: 939–57.

13. Ayton S, Lei P. *Nigral iron elevation is an invariable feature of Parkinson's disease and is a sufficient cause of neurodegeneration*. Biomed Res Int 2014.

14. Litvan, I., Goldman, J. G., Tr¨oster, A. I., Schmand, B. A., Weintraub, D., Petersen, R. Mollenhauer B, Adler CH, Marder K, Williams-Gray CH, Aarsland D, Kulisevsky J, Rodriguez-Oroz MC, Burn DJ, Barker RA, C.,Emre, M. (2012). *Diagnostic criteria for mild cognitive impairment in parkinson's disease: Movement disorder society task force guidelines*. Movement Disorders, 2012 Mar;27(3):349-56.

15. Emre M., Aarsland D., Brown R.,...and Bruno Dubois, *Clinical Diagnostic Criteria for Dementia Associated with Parkinson's Disease*. Movement Disorders Vol. 22, No. 12, 2007, pp. 1689-1707.

16. Aarsland, D., & Kurz, M. W. (2010, May). *The epidemiology of dementia associated with parkinson's disease*. Brain Pathology, 20 (3), 633-639.

17. Anderson, T., Myall, D., Wood, K., Livingston, L., Pitcher, T., Melzer, T., . . . Dalrymple-Alford, J. (n.d.). Individualised medicine: Predicting dementia in parkinsons disease.

18. T. R. Melzer, R. Watts, M. R. MacAskill, J. F. Pearson, S. Rueger, T. L. Pitcher, L. Livingston, C. Graham, R. Keenan, A. Shankaranarayanan, D. C. Alsop, J. C. Dalrymple-Alford, and T. J. Anderson, *Arterial spin labelling reveals an abnormal cerebral perfusion pattern in Parkinson's disease*, Brain 2011: 134; 845–855.

19. Tracy R Melzer, Richard Watts, Michael R MacAskill, Toni L Pitcher, Leslie Livingston, Ross J Keenan, John C Dalrymple-Alford, Tim J Anderson, *Grey matter atrophy in cognitively impaired*, J Neurol Neurosurg Psychiatry 2012;83:188-194.

20. Tracy R. Melzer, Richard Watts, , Michael R. MacAskill, Toni L. Pitcher, Leslie Livingston, Ross J. Keenan, John C. Dalrymple-Alford, Tim J. Anderson, *White matter microstructure deteriorates across cognitive stages in Parkinson disease*, Neurology 80 1841-49. May 14, 2013.

21. Goetz, C. G., Fahn, S., Martinez-Martin, P.; Poewe, W., Sampaio, C.; Stebbins, G. T.; Stern, M. B., Tilley, B. C., Dodel, R., Dubois, B., Holloway, R., Jankovic, J., Kulisevsky, J., Lang, A. E., Lees, A., Leurgans, S., LeWitt, P. A., Nyenhuis, D., Olanow, C. W., Rascol, Olivier, Schrag, A., Teresi, J. A., Van Hilten, J. J., LaPelle, N. *Movement Disorder Society-sponsored revision of the Unified Parkinson's Disease Rating Scale (MDS-UPDRS): Process, format, and clinimetric testing plan*. Movement Disorders. 22 (1): 41–47. 2007.

22. Wood, K.-L., Myall, D. J., Livingston, L., Melzer, T. R., Pitcher, T. L., MacAskill, M. R., …Dalrymple-Alford, J. C. (2016). Different pd-mci criteria and risk of dementia in Parkinson's disease: 4-year longitudinal study. npj Parkinson's Disease, 2.

23. John F. Schenck (1993). *The role of magnetic susceptibility in magnetic resonance imaging: MRI magnetic compatibility of the first and second kinds*. Medical Physics. 23: 815–850. 1996.

24. L. C. Jackson, *Investigations on paramagnetism at low temperatures,* Philos. Trans. A 224, 1-48 (1923).

25. Freude D., *Spectroscopy*, 2006, Ch. 4, pg. 1-5.

26. Haacke, E., Brown, R., Thompson, M., & Venkatesan, R. *Magnetic Resonance Imaging: Physical Principles and Sequence Design* (1st ed.). 1999. Wiley-Liss.

27. Bushong, S. C., Clarke G., *Magnetic Resonance Imaging: Physical and Biological Principles,* 2003, pg. 4, 10, 12. Mosby**.**

28. McRobbie, D., Moore, E., Graves, M., & Prince, M. (2007). *MRI From Picture to Proton* (2nd ed.). Cambridge: Cambridge University Press.

29. Pooley, R. *AAPM/RSNA Physics Tutorial for Residents: Fundamental Physics of MR Imaging*. RadioGraphics , 2005, pg. 1087-1099.

30. Edelman, R., Hesselink, J., Zlatkin, M., & Crues, J. (Eds.). (2006). *Clinical Magnetic Resonance Imaging* (3rd ed., Vol. 1). Philadelphia, PA: Saunders.

31. Peter Blümler, Siegfried Hafner, *Nuclear Magnetic Resonance, Imaging of Polymers*, Encyclopedia of Analytical Chemistry, 2009.

32. Magnitude and phase images, http://mri-q.com/uploads/3/4/5/7/34572113/7316167_orig.gif?327, accessed on 28/04/17

33. Magnetic susceptibility artefact, https://s-media-cache-ak0.pinimg.com/236x/db/97/d6/db97d686572e031c9927a840967ab092.jpg, accessed on the 30/08/16.

34. T2 contrast http://www.revisemri.com/questions/basicphysics/t2contrast, accessed on 01/09/14

35. T. Liu, C. Wisnieff, M. Lou, W. Chen, P. Spincemaille and Y. Wang, *Nonlinear Formulation of the Magnetic Field to Source Relationship for Robust Quantitative Susceptibility Mapping*, Magnetic Resonance in Medicine 69:467–476 (2013).

36. L. de Rochefort, T. Liu, B. Kressler, J. Liu, P. Spincemaille, V. Lebon, J. Wu and Y. Wang, *Quantitative Susceptibility Map Reconstruction from MR Phase Data Using Bayesian Regularization: Validation and Application to Brain Imaging*, Magnetic Resonance in Medicine 63:194–206 (2010).

37. M. D. Santin, M. Didier, R. Valabrègue, L. Yahia Cherif, D. García-Lorenzo, P. Loureiro de Sousa, E. Bardinet and S. Lehéricy, *Reproducibility of R2* and quantitative susceptibility mapping (QSM) reconstruction methods in the basal ganglia of healthy subjects*, NMR Biomed. (2016)**.**

38. Barbosa JH, Santos AC, Tumas V, Liu M, Zheng W, Haacke EM, Salmon CE. *Quantifying brain iron deposition in patients with Parkinson's disease using quantitative susceptibility mapping, R2 and R2**. Magn Reson Imaging. 2015 Jun;33(5):559-65.

39. Du G., Liu T., Lewis M.M., Kong L., Wang Y., Connor J., Mailman R.B., Huang X., *Quantitative susceptibility mapping of the midbrain in Parkinson's disease*. Mov. Disord. 2016. Vol. 31, No.3 317-24.

40. Guan X., M. Xuan, Q. Gu, P. Huang, C. Liu, N. Wang, X. Xu, W. Luo and M. Zhang, *Regionally progressive accumulation of iron in Parkinson's disease as measured by quantitative susceptibility mapping*, NMR Biomed. (2016).

41. He N., H. Ling, B. Ding, J. Huang, Y. Zhang, Z. Zhang, C. Liu, K. Chen and F. Yan, *Region-Specific Disturbed Iron Distribution in Early Idiopathic Parkinson's Disease Measured by Quantitative Susceptibility Mapping*, Human Brain Mapping 36:4407–4420 (2015).

42. J. Acosta-Cabronero, A. Cardenas-Blanco, M. J. Betts, M. Butryn, J. P. Valdes-Herrera, I. Galazky and P. J. Nestor, *The whole-brain pattern of magnetic susceptibility perturbations in Parkinson's disease*, Brain (2017) 140 (1): 118-131.

43. T. Liu et al., *Morphology enabled dipole inversion (MEDI) from a single-angle acquisition: comparison with COSMOS in human brain imaging.* MRM 2011;66(3):777-83.

44. J. Liu et al., *Morphology enabled dipole inversion for quantitative susceptibility mapping using structural consistency between the magnitude image and the susceptibility map.* Neuroimage 2012;59(3):2560-8.

45. Zhou et al., *Background field removal by solving the Laplacian boundary value problem*, NMR in Biomed 27 (3), 312-319, 2014.

46. Gelman A., Hill J. & M. Yajima, *Why We (Usually) Don't Have to Worry About Multiple Comparisons*. Journal of Research on Educational Effectiveness Volume 5, 2012 - Issue 2 Pages 189-211.

47. Almuqbel M., Melzer T. R., Myall D. J.,. MacAskill M. R, Pitcher T. L., Livingston L., Wood K.-L., Keenan R. J., Dalrymple-Alford J. C., Anderson T. J., *Metabolite ratios in the*

posterior cingulate cortex do not track cognitive decline in Parkinson's disease in a clinical setting, Parkinsonism & Related Disorders. Volume 22, Pages 54–61. Elsevier 2016.

48. Matthew J. Betts, Julio Acosta-Cabronero, Arturo Cardenas-Blanco, Peter J. Nestor, Emrah D¨uzel, *High-resolution characterisation of the aging brain using simultaneous quantitative susceptibility mapping (QSM) and R2* measurements at 7 T*. NeuroImage 2016 Volume 138, September 2016, Pages 43–63.

49. Winkler, A. M., Ridgway, G. R., Webster, M. A., Smith, S. M., & Nichols, T. E. . *Permutation inference for the general linear model*. NeuroImage, (2014) 92 , 381-397.

50. Jin L, Wang J, Zhao L, Jin H, Fei G, Zhang Y, Zeng M, Zhong C (2011): *Decreased serum ceruloplasmin levels characteristically aggravate nigral iron deposition in Parkinson's disease*. Brain 134:50–58.

51. Devos D, Moreau C, Devedjian JC, Kluza J, … Cabantchik ZI, Bordet R (2014): *Targeting chelatable iron as a therapeutic modality in Parkinson's disease*. Antioxid Redox Signal 21:195–210.

(References were cited using Vancouver style and were organised in the order that they were used)

Appendix A: Additional Analyses

	Region	Estimate (ppm)	Estimate Error (ppm)	lower 95% (ppm)	upper 95% (ppm)
	Intercept	0.006	0.005	-0.005	0.016
PDN	Left caudate	-0.004	0.006	-0.016	0.008
	Left GP	-0.001	0.006	-0.013	0.012
	Left putamen	-0.003	0.006	-0.016	0.009
	Left RN	0.008	0.007	-0.005	0.022
	Left SNc	0.020	0.008	0.005	0.037
	Left SNr	0.011	0.007	-0.003	0.026
	Left thalamus	-0.004	0.006	-0.017	0.009
	Right caudate	-0.005	0.006	-0.019	0.007
	Right GP	0.000	0.006	-0.013	0.012
	Right putamen	-0.003	0.006	-0.016	0.009
	Right RN	0.002	0.007	-0.012	0.015
	Right RSNc	0.013	0.007	-0.000	0.028
	Right SNr	0.004	0.007	-0.009	0.017
	Right thalamus	-0.005	0.006	-0.018	0.008
PD-MCI	Left caudate	-0.003	0.006	-0.014	0.008
	Left GP	0.000	0.006	-0.011	0.012
	Left putamen	-0.005	0.006	-0.017	0.005
	Left RN	-0.007	0.006	-0.020	0.004
	Left SNc	0.011	0.007	-0.001	0.025
	Left SNr	0.004	0.006	-0.008	0.016
	Left thalamus	-0.005	0.006	-0.017	0.006
	Right caudate	-0.006	0.006	-0.017	0.005
	Right GP	0.004	0.006	-0.007	0.016
	Right putamen	-0.003	0.006	-0.015	0.008
	Right RN	-0.009	0.006	-0.021	0.003
	Right RSNc	0.010	0.006	-0.001	0.023
	Right SNr	0.002	0.006	-0.009	0.013
	Right thalamus	-0.003	0.006	-0.015	0.009
	Left caudate	-0.001	0.008	-0.017	0.014
	Left GP	0.003	0.008	-0.012	0.02
	Left putamen	-0.003	0.008	-0.019	0.013
	Left RN	-0.006	0.008	-0.024	0.009
	Left SNc	0.001	0.008	-0.014	0.018
	Left SNr	0.000	0.008	-0.015	0.016
	Left thalamus	0.002	0.008	-0.013	0.020

PDD	Right caudate	-0.004	0.008	-0.021	0.011
	Right GP	0.006	0.009	-0.010	0.024
	Right putamen	-0.003	0.008	-0.019	0.012
	Right RN	0.005	0.008	-0.023	0.011
	Right RSNc	-0.001	0.008	-0.017	0.015
	Right SNr	0.005	0.008	-0.022	0.010
	Right thalamus	0.004	0.008	-0.012	0.021

Table A1: Complete data for the category analysis.

Region	**Estimate (ppm)**	**Estimate Error (ppm)**	**Lower 95% (ppm)**	**Upper 95% (ppm)**
Intercept	0.006	0.005	-0.004	0.016
Left caudate	-0.006	0.006	-0.018	0.005
Left GP	-0.001	0.006	-0.014	0.011
Left putamen	-0.011	0.007	-0.026	0.002
Left RN	0.005	0.007	-0.008	0.018
Left SNc	0.024	0.008	0.009	0.040
Left SNr	0.015	0.007	0.001	0.030
Left thalamus	-0.006	0.007	-0.020	0.006
Right caudate	-0.007	0.007	-0.021	0.005
Right GP	0.001	0.007	-0.012	0.014
Right putamen	-0.009	0.007	-0.023	0.003
Right RN	0.005	0.007	-0.008	0.020
Right RSNc	0.023	0.008	0.008	0.038
Right SNr	0.010	0.007	-0.004	0.024
Right thalamus	-0.004	0.007	-0.017	0.009

Table A2: Group model from the CogZ analysis.

Region	Estimate (ppm)	Estimate Error (ppm)	Lower 95% (ppm)	Upper 95% (ppm)
Intercept	0.002	0.005	-0.009	0.012
Left caudate	-0.001	0.012	-0.026	0.023
Left GP	0.005	0.013	-0.017	0.038
Left putamen	0.001	0.012	-0.022	0.027
Left RN	0.003	0.012	-0.020	0.031
Left SNc	0.010	0.016	-0.013	0.050
Left SNr	0.007	0.015	-0.016	0.041
Left thalamus	-0.001	0.012	-0.026	0.023
Right caudate	-0.005	0.013	-0.036	0.019
Right GP	-0.001	0.013	-0.029	0.023
Right putamen	-0.001	0.012	-0.027	0.023
Right RN	-0.004	0.013	-0.034	0.019
Right SNc	-0.003	0.013	-0.032	0.021
Right SNr	-0.004	0.013	-0.033	0.019
Right thalamus	0.000	0.012	-0.025	0.025

Table A3: Results of UPDRS-II model for mean QSM.

Region	Estimate (ppm)	Estimate Error (ppm)	Lower 95% (ppm)	Upper 95% (ppm)
Intercept	0.002	0.005	-0.008	0.012
Left caudate	0.011	0.016	-0.014	0.051
Left GP	0.005	0.013	-0.018	0.035
Left putamen	-0.005	0.014	-0.037	0.020
Left RN	0.001	0.012	-0.022	0.025
Left SNc	-0.002	0.012	-0.028	0.022
Left SNr	0.001	0.013	-0.024	0.028
Left thalamus	-0.003	0.013	-0.029	0.020
Right caudate	0.002	0.013	-0.023	0.029
Right GP	0.001	0.012	-0.024	0.025
Right putamen	-0.007	0.015	-0.044	0.017
Right RN	-0.003	0.013	-0.032	0.021
Right SNc	-0.008	0.015	-0.044	0.016
Right SNr	0.002	0.012	-0.023	0.027
Right thalamus	0.002	0.005	-0.008	0.012

Table A4: Results of UPDRS-III model for mean QSM.

Region	Estimate (ppm)	Estimate Error (ppm)	Lower 95% (ppm)	Upper 95% (ppm)
Intercept	0.001	0.005	-0.009	0.012
Left caudate	-0.002	0.013	-0.029	0.024
Left GP	0.007	0.015	-0.017	0.042
Left putamen	-0.007	0.013	-0.040	0.015
Left RN	0.013	0.018	-0.014	0.062
Left SNc	0.007	0.015	-0.016	0.044
Left SNr	-0.004	0.013	-0.033	0.019
Left thalamus	-0.001	0.013	-0.028	0.023
Right caudate	-0.007	0.015	-0.046	0.016
Right GP	0.004	0.013	-0.018	0.036
Right putamen	-0.003	0.013	-0.031	0.020
Right RN	0.002	0.013	-0.023	0.028
Right SNc	0.004	0.013	-0.019	0.035
Right SNr	-0.009	0.015	-0.045	0.016
Right thalamus	-0.005	0.014	-0.035	0.019

Table A5: Results of the disease duration model for mean QSM.